




## Generalized universal equation of states for magnetic materials: A novel formulation for an interatomic potential in Fe

Isaac Toda-Caraballo <sup>1,\*</sup>, Jan S. Wróbel <sup>2</sup> and Duc Nguyen-Manh <sup>3,4</sup>

<sup>1</sup>*Materialia Group/Physical Metallurgy Department, National Center for Metallurgical Research (CENIM-CSIC), Avda. Gregorio del Amo 8, Madrid 28040, Spain*

<sup>2</sup>*Faculty of Materials Science and Engineering, Warsaw University of Technology, ul. Włocławska 141, 02-507 Warsaw, Poland*

<sup>3</sup>*Culham Centre for Fusion Energy (CCFE), United Kingdom Atomic Energy Authority, Abingdon, Oxfordshire OX14 3DB, United Kingdom*

<sup>4</sup>*Department of Materials, University of Oxford, Parks Road, Oxford OX1 3PH, United Kingdom*



(Received 20 September 2021; revised 10 March 2022; accepted 29 March 2022; published 28 April 2022)

The development of quantitative models for understanding physical properties of alloys requires a proper treatment of magnetic interactions, which is of paramount importance for the microstructural stability, especially in steels and high-entropy alloys containing magnetic elements. These magnetic interactions also control the defects behavior which affects the mechanical properties and the response under irradiation. Current interatomic potentials for molecular dynamics (MD) simulations still lack an adequate formulation to include magnetism into the simulations. In this paper, the universal equation of states (UES) is revisited and generalized by including ferromagnetic (FM) and antiferromagnetic (AFM) configurations with the aim of proposing a new formulation to develop interatomic potentials with magnetic contribution. For the case of Fe, given a fixed magnetic configuration and magnitude of the magnetic moment, the energy of the system is calculated by means of three parameters, namely, the energy, volume, and corresponding scaling volume (directly related to the bulk modulus) at the local ground state of the corresponding lattice. These parameters depend on three terms: firstly, a distance-dependent function, which gathers the nonmagnetic influence of the surrounding atoms; secondly, a magnetically dependent function, contributing to the energy by means of the magnetic nature of the atom, irrespective of the magnetic moment magnitudes of its surrounding atoms; and finally, a term which is magnetically and distance dependent simultaneously, which describes the influence of the magnetic state of the surrounding atoms on the energy considering their interatomic distance. This latter term is built via two functions which cannot be disconnected: one dependent on the distance between two atoms (a decreasing function with the distance in absolute value) multiplied by another function which is dependent on the magnetic moment of these two atoms. In this way, the magnetic influence of a distant atom scales with its distance. The new formulation is tested for magnetic iron, where 18 240 spin polarized density functional theory (DFT) calculated energies for different lattices, volumes, and magnetic moments in FM and AFM configurations showed that the generalized UES (GUES) accurately describes the energy of the system. The root-mean-square error of the GUES is in the range of  $5.9 \times 10^{-3}$  eV over all DFT calculated energies, showing good accuracy and allowing us to propose a formulation for developing a magnetic interatomic potential (MIP) in Fe. The potential is developed for FM configuration in iron, aiming at studying the stability of the ferritic and austenitic phases but also defects and other configurations of special relevance as, for instance, in irradiation conditions for fusion or fission applications. The distance and magnetic functions of the GUES are tabulated to obtain a MIP, which describes the DFT calculated energies for different lattices, volumes, and magnetic moments in FM configuration. Further, the MIP has been validated in other crystal lattices (A15 and C15), elastic constants, stresses in the lattice, vacancies, interstitials, forces at different temperatures, transformation paths between body-centered cubic, face-centered cubic, hexagonal close-packed, and simple cubic structures as well as  $\gamma$  surfaces. We conclude that the results in this paper pave the way to develop MIPs with accuracy and predictability beyond the state of the art in MD.

DOI: [10.1103/PhysRevMaterials.6.043806](https://doi.org/10.1103/PhysRevMaterials.6.043806)

### I. INTRODUCTION

During the early conception of the atomistic simulations, different approaches were postulated to perform molecular dynamics (MD) simulations in metals. Semiempirical poten-

tials based on the embedded atom method (EAM) [1,2] or many-body force potential [3,4] were developed to fit relevant properties or were optimized [5] to fit density functional theory (DFT) calculations. This allowed tremendous advances in the analysis of atomic interactions, providing exceptional tools to investigate key parameters [6–8]. Nevertheless, classical MD interatomic potentials frequently lacked the influence of magnetism. This influence is generally embedded in the

\*Corresponding author: isaac.toda@cenim.csic.es

energy description and the ground state configurations as an underlying property which cannot be evaluated [9–14]. For the case of iron, it is nevertheless important to stress that most of the developed potentials accurately describe body-centered cubic (BCC) structures and their vicinities, including face-centered cubic (FCC) structures, being potentials that predict the energy in the ferromagnetic (FM) configuration, without describing the magnetic contribution. In this way, potentials were conceived describing  $\alpha$ -Fe and its modifications, where the energy, elastic constants, forces, or the behavior of the lattice in the presence of defects are correctly approximated, being under the influence of magnetism [15,16] but without particular information about the possible magnetic fluctuations that may occur. Other potentials in binary Fe systems can describe precipitation and point defects [17], liquid and crystalline iron, along with its elastic constants, point-defect energies as well as BCC-FCC transformation energy [18] or C diffusion in a low C-concentrated Fe system [19]. Therefore, the lack of magnetism in these formulations does not discredit the tremendous advances possible thanks to these interatomic potentials which enabled many correct calculations, especially if the magnetic fluctuations were small enough. Thus, these potentials work nicely in the surroundings of the ground state, but they cannot describe the atomic interactions in a general way.

Previous *ab initio* studies based on spin-polarized DFT calculations demonstrated clearly that the magnetic contribution plays a crucial role in determining not only structural stability of ground states but also metastable phases and defect properties for Fe as well as for iron-based alloys including new high-entropy ones [20–32]. It is found from our DFT systematic study of group-specific trends for self-interstitial atom (SIA) defects in BCC transition metals that, while the lowest-energy SIA configuration for the nonmagnetic (NM) metals in groups 5B and 6B of the periodic table is the crowdion or  $\langle 111 \rangle$  dumbbell, the predicted most stable SIA defect configuration in FM Fe is the  $\langle 110 \rangle$  dumbbell [21–23,26,27,33]. The magnetic origin of the relative stability between SIA defect configurations can be explained from the quantum-mechanical based tight-binding Stoner model [34–36], which forms the theoretical background for the development of magnetic bond order potential (BOP) for Fe [37].

DFT calculations have shown that the behavior of 3d-series transition metals in a crystal lattice depends deeply on the magnetic configuration of its atoms. For instance, the value of the magnetic moment of atoms along defects differs strongly and depends on their position and atomic volume in the lattice [38]. Additionally, and following the example of iron, the modeling of a phase transformation to NM FCC or hexagonal close-packed (HCP) from magnetic BCC is challenging from the physical point of view, as the factor responsible for that transformation, the magnetic configuration, is not described [20,29,39,40]. Some recent DFT calculations on the FeCrNi [29] and CoCrNi [41,42] systems have displayed the strong variation of the magnetic moment by means of the composition and crystal structure considered, explaining the experimentally observed ground state. As the compositional complexity increases, for instance, in the high-entropy alloys (HEAs), the variations in magnetic configurations are even stronger [43], and the atoms can modify their magnetic config-

uration with small variations in composition. For example, in Ref. [31], it is shown that, depending on alloy composition, the FeCrMnNi alloys can have FM, ferrimagnetic, antiferromagnetic (AFM), or NM configurations. In other cases, NM elements such as Pd became magnetic in the matrix, as in the CoCrFeNi-Pd system [30], changing their behavior dramatically. All these variations affect the entropy of the system, which in turn influences the stability and the ground state configurations [31,44]. The study of magnetism is also of paramount importance in the development of materials for nuclear plants, both fission and fusion, where the interatomic interactions for modeling radiation damage depends strongly on the magnetic behavior of the materials, especially in iron alloys [45]. The need to investigate irradiation damage in collision cascades and how vacancies, SIAs, and defect clusters evolve is well documented and related to both magnetic and atomic degrees of freedom [27].

Therefore, the exploration of approaches to investigate magnetism in MD simulations has gained attention during the last few years. Some works have managed to include the magnetic influence using, for instance, BOP and angular-dependent functional forms to reproduce the  $\alpha$ -iron to  $\gamma$ -iron transition at high temperature [37,46,47]. In those works, BOP and analytical BOP (ABOP) showed clear improvements with respect to empirical potentials, which do not include the magnetism in their formulation, predicting an energy barrier between the  $\alpha$ -iron and  $\gamma$ -iron. Nevertheless, the predicted energies displayed substantial differences when compared with DFT results. Taking the EAM as a starting point, some other achievements have been made introducing a physical description of the magnetism into the potential [45,48,49] by using a combination of the Stoner model of band magnetism [50] and the approximation proposed by the Ginzburg-Landau model [51]. The variations of magnetic moments are locally well described, including different interstitial configurations and dislocations loops, but it is not a formulation to cover from NM to magnetic configurations in a wide spectrum of crystal structures. The large-scale spin-lattice dynamics (SLD) algorithm [52] has also been investigated with success, allowing the magnetic moment to be studied as a function of the temperature. Other works [40] developed the noncollinear magnetic many-body potentials for BCC and FCC iron by combining NM many-body potentials and Heisenberg-Landau Hamiltonians for BCC and FCC iron. The potential was next applied in SLD simulations to evaluate the difference between the free energies of BCC and FCC phases. With the advent of novel machine learning interatomic potential models [53], more recent approaches such as the magnetic moment tensor potentials showed that this technique can be applied to reproduce with accuracy DFT data as well as the local magnetic moments, energies, and forces for various magnetic states along with high computational efficiency [54]. This technique nevertheless is always subjected to the machine learning paradigm, where the method does not capture the laws of physics, providing little understanding of the interatomic interactions, even though high accuracy is obtained.

It is evident that the current MD potentials and approaches have difficulties in capturing the magnetic interactions and transferring such complexity into the calculation of the energies. The previous examples of interatomic potentials

correspond to different proposals for atom-atom interactions, which are oriented to a certain structure or property, and are less accurate for other situations where alternative potentials succeed. Therefore, there is not yet a unique interatomic potential formulation, while the actual underlying atom-atom interactions are uniquely defined by the laws of physics.

In this paper, we have revisited the universal equation of states (UES) formulation to evaluate the nature of the magnetic influence. With this, we ideally aim at starting a path that could lead to a general formulation of the atomic interactions for MD simulations. This paper corresponds indeed to a theoretical one, where the calculations of the energy are performed using the spin-polarized DFT approach. Starting from the principle that the DFT calculations need to be contrasted with experiments, as any other model employed, this approximation is considered correct and represents faithfully the energy dependence of a certain crystal lattice, magnetic moment, and magnetic configuration. Many previous works using DFT validate this affirmation. On the other hand, DFT calculations can provide information that cannot be obtained by experiments such as nonequilibrium configurations. This is an advantage extremely useful for the fitting of potentials.

The objective of this paper is to propose a novel formulation that can be used for developing a magnetic potential for MD simulations. The UES proposed by Rose *et al.* [55] and Vinet *et al.* [56] is used as a base functional and employed firstly to analyze the behavior of the energy at different crystal lattices, volumes, and importantly, the magnetic moments at different magnetic configurations, which generalizes the use of the UES. This generalized universal equation of states (GUES) is tested in pure iron with FM and AFM contributions, and it can reproduce the energy of a wide spectrum of crystal lattices that have been calculated from first principles. Nevertheless, the incorporation of all possible magnetic configurations into an interatomic potential is a task of large complexity, making it unreasonable in the first stage to face it. We attempt initially at understanding ferromagnetism and antiferromagnetism, which play a central role in physical metallurgy and particularly in iron. Other forms of magnetism as ferrimagnetic or paramagnetic configurations are still out of the scope of this paper and deserve additional investigations.

Because of this approach, a novel magnetic interatomic potential (MIP) is formulated based on the GUES. It is important to note that the GUES predicts different magnetic functional forms for each magnetic configuration, and correspondingly, the MIP proposed in this paper is focused on ferromagnetism for its great relevance in Fe and in other metals. The developed MIP has been put to the test to describe the behavior of several structures and properties which were not initially included in the fitting procedure, showing good predictability.

The paper is structured as follows. Section II formulates the equations of the MIP based on a generalization of the UES. Section III describes the database employed and the nature of DFT calculations used along the paper. Section IV analyzes the behavior of the parameters by means of crystal structure and magnetic moment and the fitting of the potential, finishing with the proposed functional forms proposed to be used for the MIP as well as the functions and equations for the MIP with FM configuration. Section V validates the potential in the original DFT calculated energies for a wide range of

crystal lattices, volumes, and magnetic moment magnitudes and analyzes the predictability of the potential in different parameters and structures, including elastic constants, stresses in the lattice, forces for different temperatures, vacancies, interstitials, and transformation paths as well as  $\gamma$  surfaces. Finally, Sec. VI contains the conclusions.

## II. MIP FORMULATION BASED ON THE GUES

The UES [55,56] determines that there is a unique function that describes the behavior of the energy for all solids with respect to volume variations. The use of the UES has been extensively validated in the literature and successfully applied to predict material properties related to volume change [16,57–63]. Other works have proposed empirical equations of states where the parameters are fitted to provide the best fit to experiments [64–68] but without developing an interatomic potential from the proposed equations.

That approach is originally expressed via the distance between atoms or the Wigner-Seitz radius. This interatomic distance in turn scales with the atomic volume since the distance in the formulation is understood as the cell parameter, and its variation induces a change in the atomic volume. The atomic volume is in fact a more relevant parameter to explain relationships between atoms [69] and thermodynamics [70] of metals and alloys. Additionally, it will be shown that the formulation using the volume allows relating directly the parameters obtained in the approach with measurable parameters, such as the bulk modulus (explained below), but also to express the volume variations directly during the simulation. More importantly, the magnetic moment is directly related to the volume [29], and therefore, a formulation based on volume rather than in interatomic distances provides clear advantages for including magnetism. Both the Wigner-Seitz radius and the atomic volume in the UES provides a very accurate fitting to the energy after cell variations, and a short comparison between both will be included in Sec. IV when the UES is validated.

Therefore, in this paper, we have adopted the atomic volume  $V$  as the main parameter in the UES rather than the distance between atoms. With this approach, the functions  $F$  that define the UES read then

$$F(V^*) = e^{-V^*}(1 + V^*), \quad (1)$$

where  $V^*$  is the scaled volume, defined in the same fashion as in [56]

$$V^* = \frac{V - V_g}{K_g}, \quad (2)$$

where  $V_g$  is the volume at the ground state and  $K_g$  the corresponding volume scaling function. Thus, the Rose *et al.* [55] and Vinet *et al.* [56] expression of the energy  $E$  as a function of volume  $V$  is expressed as

$$E(V) = E_g F\left(\frac{V - V_g}{K_g}\right) = E_g \exp\left(-\frac{V - V_g}{K_g}\right) \left(1 + \frac{V - V_g}{K_g}\right). \quad (3)$$

In this equation,  $E_g$  is the ground state energy, which is like the equilibrium binding energy proposed in Ref. [56] denoted originally  $\Delta E$ . The  $V_g$  and  $K_g$  parameters correspond

to  $r_{\text{WSE}}$  (Wigner-Seitz equilibrium radius) and  $l$  (length scale) as defined in Ref. [56], respectively.

The use of the term *ground state* to define  $E_g$ ,  $V_g$ , and  $K_g$  must be more general in this paper, as these parameters correspond to the local ground state energy and corresponding local ground state volume for each crystal lattice considered. In other words, the ground states for BCC and FCC lattices are logically different and provide different values of  $E_g$ ,  $V_g$ , and  $K_g$ . Therefore, the defined  $E_g$ ,  $V_g$ , and  $K_g$  parameters vary for each of the crystal lattices. Based on this approach and Eq. (3), a formulation for a MIP is developed here, where the values of  $E_g$ ,  $V_g$ , and  $K_g$  must be predicted for the corresponding crystal configuration. It is worth noting that these parameters depend on the crystal lattice and the magnetic moment configuration, but they must be independent of volume  $V$  to fulfill the UES. A dedicated subsection is presented later in Sec. IV B devoted to the description and understanding of the potential parameters  $E_g$ ,  $V_g$ , and  $K_g$ .

To adequately formulate the potential, a prior definition of the variables involved must be presented. Firstly, the interatomic distance between atoms  $r_{ij} = \sqrt{x_{ij}^2 + y_{ij}^2 + z_{ij}^2}$ , where  $x_{ij} = x_i - x_j$ ,  $y_{ij} = y_i - y_j$ , and  $z_{ij} = z_i - z_j$  are the relative coordinates between two atoms, and  $(x_i, y_i, z_i)$  and  $(x_j, y_j, z_j)$  are the corresponding spatial coordinates of atoms  $i$  and  $j$ , respectively. Secondly, the magnetic moment of each atom  $M_i$  represents the magnitude of the magnetic moment in the FM and AFM configurations. Finally, the atomic volume  $V$  must be understood as a bulk quantity and not the volume per atom individually. This is itself a novelty in the present scope of interaction between atoms since the volume is not considered a variable in classical approaches for interatomic potentials.

The variables, as they are presented, are not fully independent of each other since the interatomic distance  $r_{ij}$  and the volume  $V$  are related. From the point of view of the UES presented in Eq. (3), taking a certain lattice, a variation on its volume (expansion or contraction) follows a change in the atomic coordinates, which induces the corresponding alteration in the interatomic distance between atoms. Therefore, a variable of this nature cannot be used to describe  $E_g$ ,  $V_g$ , and  $K_g$  since the dependence of these functions cannot include the volume, which would break the UES in Eq. (3). Therefore, a variable related to the atomic coordinates but independent of the volume must be considered. This is the variable  $\rho_{ij}$ , corresponding to the relative interatomic distances per unit volume, which is defined as

$$\rho_{ij} = \frac{r_{ij}^3}{V}. \quad (4)$$

In Eq. (4), the variable  $\rho_{ij}$  is unitless, and represents the distances between atoms in a certain crystal lattice, no matter the volume of such lattice. In other words, two BCC lattices with different lattice constants would have different interatomic distances between atoms  $r_{ij}$ , but they both will have the same values of  $\rho_{ij}$ , no matter their cell parameter. Additionally, other crystal lattices, such as FCC, will have different  $\rho_{ij}$  with respect to the ones in BCC, but two lattices with FCC will have the same  $\rho_{ij}$  irrespective of their cell parameter, although they will have obviously different  $r_{ij}$ . This applies to any other lattice for which its relative interatomic

distances per unit volume is the same under volume variations. Therefore, the variable  $\rho_{ij}$  is independent of volume  $V$  in a certain lattice.

To lighten the notation, we will denote  $\boldsymbol{\rho}$  as a variable that accounts for the interatomic distances and represents the distance dependence on the parameters and functions that will define the potential. Similarly, we will denote  $\mathbf{M}$  as a variable that accounts for the magnetic moment magnitudes of the lattice and represents the magnetic dependence on the parameters and functions that will define the potential. The expressions of these parameters and functions with respect to interatomic distances and magnetic moments will be described in detail below.

Once the variables are introduced, the dependence of the potential parameters  $E_g$ ,  $V_g$ , and  $K_g$  must be considered. As stated above, these functions cannot be dependent on volume  $V$  since this would break the UES. The potential parameters  $E_g$ ,  $V_g$ , and  $K_g$  depend only on the relative interatomic distances per unit volume  $\rho_{ij}$  and the magnetic moment of each atom  $M_i$ . Therefore, we will denote  $E_g \equiv E_g^i(\boldsymbol{\rho}, \mathbf{M})$ ,  $V_g \equiv V_g^i(\boldsymbol{\rho}, \mathbf{M})$ , and  $K_g \equiv K_g^i(\boldsymbol{\rho}, \mathbf{M})$  using the  $\boldsymbol{\rho}$  and  $\mathbf{M}$  notation to account for the set of interatomic distances  $\rho_{ij}$  and magnetic moments  $M_i$  of the different atoms surrounding atom  $i$ , where the superscript  $i$  indicates the corresponding value of the potential parameters for the atom  $i$ . The energy  $E$  of a lattice is then calculated as the sum over all atoms  $i$  of all contributions  $E^i$  to the energy of the system, where these contributions are

$$E^i(V, \boldsymbol{\rho}, \mathbf{M}) = E_g^i(\boldsymbol{\rho}, \mathbf{M}) \exp\left[-\frac{V - V_g^i(\boldsymbol{\rho}, \mathbf{M})}{K_g^i(\boldsymbol{\rho}, \mathbf{M})}\right] \times \left[1 + \frac{V - V_g^i(\boldsymbol{\rho}, \mathbf{M})}{K_g^i(\boldsymbol{\rho}, \mathbf{M})}\right]. \quad (5)$$

In this equation, the expression  $\boldsymbol{\rho}$  refers to the interatomic distances per unit volume of atom  $i$ , while  $\mathbf{M}$  involves the magnetic moment of atom  $i$  and the magnetic moment of all its neighbors in the lattice.

It is worth noting that this equation generalizes the previous use of the UES for different crystal lattices and magnetic configurations. In the classical approach of Rose *et al.* [55] and Vinet *et al.* [56], the radius of the Wigner-Seitz sphere, represented in this case by the atomic volume  $V$ , corresponds to an average volume per atom, and it is the unique parameter to calculate the energy. The  $r_{\text{WSE}}$  (equilibrium radius) and  $l$  (length scale) as defined in Ref. [56] were reported as single values for each atom. This single value corresponds to the ground state configuration of each atomic species and not the local ground state for each lattice, as proposed here. The ground state concept is extended here to account for each lattice and magnetic configuration, which induces changes in  $E_g$ ,  $V_g$ , and  $K_g$  (respectively  $\Delta E$ ,  $r_{\text{WSE}}$ , and  $l$ ). To be consistent with the classical nomenclature, we will keep the term *ground state* to be used for the configuration corresponding to the lowest energy for an atom, whereas the term *local ground state* will be used to describe the minimum energy and volume once a lattice and magnetic configuration is fixed.

To account for this generalization, we propose the following expressions for the potential parameters  $E_g^i(\boldsymbol{\rho}, \mathbf{M})$ ,

$V_g^i(\boldsymbol{\rho}, \mathbf{M})$ , and  $K_g^i(\boldsymbol{\rho}, \mathbf{M})$ :

$$\begin{aligned} E_g^i(\boldsymbol{\rho}, \mathbf{M}) &= E_0^i(\boldsymbol{\rho}) + \Phi_E(M_i) + \sum_{j \neq i} \omega_M(\rho_{ij}) \psi_E(M_i, M_j) \\ V_g^i(\boldsymbol{\rho}, \mathbf{M}) &= V_0^i(\boldsymbol{\rho}) + \Phi_V(M_i) + \sum_{j \neq i} \omega_M(\rho_{ij}) \psi_V(M_i, M_j) \\ K_g^i(\boldsymbol{\rho}, \mathbf{M}) &= K_0^i(\boldsymbol{\rho}) + \Phi_K(M_i) + \sum_{j \neq i} \omega_M(\rho_{ij}) \psi_K(M_i, M_j), \end{aligned} \quad (6)$$

where the subscript  $j \neq i$  represents all neighbor atoms of atom  $i$ .

In the expressions shown in Eq. (6), each potential parameter depends on one distance-dependent function, denoted  $E_0^i(\boldsymbol{\rho})$ ,  $V_0^i(\boldsymbol{\rho})$ , and  $K_0^i(\boldsymbol{\rho})$ , respectively. These functions represent the NM behavior of the atom in different lattices, having the expressions:

$$\begin{aligned} E_0^i(\boldsymbol{\rho}) &= \varepsilon_{0,0} + \varepsilon_{0,1} \sum_{j \neq i} \omega_0(\rho_{ij}) \\ V_0^i(\boldsymbol{\rho}) &= \nu_{0,0} + \nu_{0,1} \sum_{j \neq i} \omega_0(\rho_{ij}) \\ K_0^i(\boldsymbol{\rho}) &= \kappa_{0,0} + \kappa_{0,1} \sum_{j \neq i} \omega_0(\rho_{ij}). \end{aligned} \quad (7)$$

The function  $\omega_0(\rho_{ij})$  is understood as the classical interatomic distance-dependent function in the EAM or other classical approaches for interatomic potentials. Note that the same function is used for the three potential parameters. The justification for the use of a common function for the three parameters will be introduced in Sec. IV B, where the DFT energies calculated will be interpreted in the scope of the GUES.

Additionally, the magnetic influence on the potential parameters is related to two different types of functions. The functions  $\Phi_E(M_i)$ ,  $\Phi_V(M_i)$ , and  $\Phi_K(M_i)$  are only dependent on the magnetic moment of the atom  $i$  and independent of the magnetic configuration of the lattice. The influence of the magnetic configuration of the lattice is introduced by means of the functions  $\sum_{j \neq i} \omega_M(\rho_{ij}) \Psi(M_i, M_j)$ , where the function  $\Psi$  represents correspondingly  $\Psi_E$ ,  $\Psi_V$ , and  $\Psi_K$ . The magnetic influence of the lattice on an atom  $i$  is decoupled into pair contributions between atoms  $j$  (in the lattice) and atom  $i$ , in the form of  $\omega_M(\rho_{ij}) \Psi(M_i, M_j)$ . In this way, the magnetic influence of atom  $j$  on  $i$  decreases with the distance between both, thanks to the distance-dependent function  $\omega_M(\rho_{ij})$ . The magnetically dependent functions  $\Psi_E(M_i, M_j)$ ,  $\Psi_V(M_i, M_j)$ , and  $\Psi_K(M_i, M_j)$  are then defined by means of the magnetic moments  $M_i$  and  $M_j$  of both atoms. Like in the case of the  $\omega_0(\rho_{ij})$  function, a unique expression of the distance-dependent function  $\omega_M(\rho_{ij})$  is used for the three parameters, which will be justified in Sec. IV B. The analysis performed in that section will pave the way to define and predict  $\omega_0$ ,  $\omega_M$  distance-dependent functions, and  $\Phi$ ,  $\Psi$  magnetically dependent functions. Note that all  $\Phi$ ,  $\Psi$  functions equal 0 when the magnetic moment is 0, leaving in this way the NM description only to  $E_0^i(\boldsymbol{\rho})$ ,  $V_0^i(\boldsymbol{\rho})$ , and  $K_0^i(\boldsymbol{\rho})$ .

This proposed formulation is consistent with the Heisenberg-Landau Hamiltonian used for magnetic cluster expansion simulations [28], where the  $E_0^i(\boldsymbol{\rho})$ ,  $V_0^i(\boldsymbol{\rho})$ , and  $K_0^i(\boldsymbol{\rho})$  parameters are related to the NM cluster expansion coefficients, the  $\Phi_E(M_i)$ ,  $\Phi_V(M_i)$ , and  $\Phi_K(M_i)$  magnetically dependent functions correspond to the Landau coefficients for the magnetic self-energy terms, while  $\Psi_E(M_i, M_j)$ ,  $\Psi_V(M_i, M_j)$ , and  $\Psi_K(M_i, M_j)$ , scaled by  $\omega_M(\rho_{ij})$ , represent the lattice magnetic configuration described by the interlattice-site Heisenberg magnetic interaction parameters. Because of the analysis performed below in Sec. IV B, these functions are approximated using polynomial expressions of the magnetic moments. This is also in line with the defined magnetic dependence proposed in the Heisenberg-Landau Hamiltonian.

For the proposed formulation, the derivation of the equations for molecular static simulations has been carried out. To lighten the mathematical expressions and without loss of generality, we will avoid the explicit expression of each dependence in the functions, adopting the notation  $E_g^i \equiv E_g^i(\boldsymbol{\rho}, \mathbf{M})$ ,  $V_g^i \equiv V_g^i(\boldsymbol{\rho}, \mathbf{M})$ , and  $K_g^i \equiv K_g^i(\boldsymbol{\rho}, \mathbf{M})$  as well as for the distance-dependent functions  $\omega_0 \equiv \omega_0(\rho_{ij})$  and  $\omega_M \equiv \omega_M(\rho_{ij})$  and the magnetically dependent functions  $\Phi \equiv \Phi(M_i)$  and  $\Psi \equiv \Psi(M_i, M_j)$ . Additionally, let  $\xi_{ij} \equiv x_{ij}$ ,  $y_{ij}$ , or  $z_{ij}$ . With this, the derivatives of the energy with respect to the atomic coordinates, magnetic moment, and volume read

$$\begin{aligned} \frac{\partial E^i}{\partial \xi_{ij}} &= \frac{\partial E^i}{\partial \rho_{ij}} \frac{\partial \rho_{ij}}{\partial \xi_{ij}} = \exp\left(-\frac{V - V_g^i}{K_g^i}\right) \left\{ \frac{\partial E_g^i}{\partial \rho_{ij}} \left(1 + \frac{V - V_g^i}{K_g^i}\right) \right. \\ &\quad \left. + \frac{\partial K_g^i}{\partial \rho_{ij}} \left[ \frac{E_g^i}{K_g^i} \left(\frac{V - V_g^i}{K_g^i}\right)^2 \right] + \frac{\partial V_g^i}{\partial \rho_{ij}} \frac{E_g^i (V - V_g^i)}{K_g^{i2}} \right\} 3\xi_{ij} \frac{r_{ij}}{V} \\ \frac{\partial E^i}{\partial M_i} &= \frac{E^i}{E_g^i} \frac{\partial E_g^i}{\partial M_i} + \left[ E - E_g^i \exp\left(-\frac{V - V_g^i}{K_g^i}\right) \right] \\ &\quad \times \left( \frac{\partial V_g^i}{\partial M_i} + \frac{\partial K_g^i}{\partial M_i} \frac{V - V_g^i}{K_g^i} \right) \frac{1}{K_g^i} \\ \frac{\partial E^i}{\partial V} &= \left[ E_g^i \exp\left(-\frac{V - V_g^i}{K_g^i}\right) - E \right] \frac{1}{K_g^i}, \end{aligned} \quad (8)$$

where the explicit expression of the variation of  $E_g^i$ ,  $V_g^i$ , and  $K_g^i$  with respect to  $\rho_{ij}$  and  $M_i$  as well as the derivative  $\rho_{ij}$  with respect to the atomic coordinates are needed. This can be easily calculated from Eqs. (6) and (7) as

$$\begin{aligned} \frac{\partial E_g^i}{\partial \rho_{ij}} &= \varepsilon_{0,2} \sum_{j \neq i} \frac{d\omega_0}{d\rho_{ij}} + \sum_{j \neq i} \frac{d\omega_M}{d\rho_{ij}} \Psi_E \\ \frac{\partial V_g^i}{\partial \rho_{ij}} &= \nu_{0,2} \sum_{j \neq i} \frac{d\omega_0}{d\rho_{ij}} + \sum_{j \neq i} \frac{d\omega_M}{d\rho_{ij}} \Psi_V \\ \frac{\partial K_g^i}{\partial \rho_{ij}} &= \kappa_{0,2} \sum_{j \neq i} \frac{d\omega_0}{d\rho_{ij}} + \sum_{j \neq i} \frac{d\omega_M}{d\rho_{ij}} \Psi_K \\ \frac{\partial E_g^i}{\partial M_i} &= \frac{d\Phi_E}{dM_i} + \sum_{j \neq i} \omega_M \frac{\partial \Psi_E}{\partial M_i} \end{aligned}$$

$$\begin{aligned}
\frac{\partial V_g^i}{\partial M_i} &= \frac{d\Phi_V}{dM_i} + \sum_{j \neq i} \omega_M \frac{\partial \Psi_V}{\partial M_i} \\
\frac{\partial K_g^i}{\partial M_i} &= \frac{d\Phi_K}{dM_i} + \sum_{j \neq i} \omega_M \frac{\partial \Psi_K}{\partial M_i} \\
\frac{\partial \rho_{ij}}{\partial \xi_{ij}} &= 3\xi_{ij} \frac{r_{ij}}{V}.
\end{aligned} \tag{9}$$

Equation (5) together with Eqs. (6) and (7) represent the MIP presented here. This formulation is drawn from the analysis performed in the numerically fitted functions  $E_g^i(\boldsymbol{\rho}, \mathbf{M})$ ,  $V_g^i(\boldsymbol{\rho}, \mathbf{M})$ , and  $K_g^i(\boldsymbol{\rho}, \mathbf{M})$  from the DFT simulations. After the initial fitting, an analysis of the dependence of these functions with respect to  $\boldsymbol{\rho}$  and  $\mathbf{M}$  allowed formulating Eqs. (6) and (7). A detailed analysis of these parameters and how these equations are proposed will be shown in Sec. IV. The study of their behavior with respect to different lattices and different magnetic moments has been crucial in the understanding of the mathematical expressions needed to describe them. The DFT calculations are presented in Sec. III, and the corresponding analysis is shown in Sec. IV B.

Additionally, Eqs. (8) and (9) represent the equation of motion of the MIP, where the motion is understood not only in the atomic coordinates but also in the magnetic moments. It is obvious that the speed at which the atomic coordinates and the magnetic moments vary can be different since the magnetic moment is related to the electrons of the moving atoms, working in this way at different length and time scales. Nevertheless, it is out of the scope of this paper to analyze properly the variational speed and scale of each parameter.

### III. DATABASE AND DFT CALCULATIONS

The interatomic potential for Fe was parametrized based on the DFT calculations, which were performed using the Vienna *Ab initio* Simulation Package (VASP) [71,72] using the projector augmented-wave (PAW) method [73] and the Perdew-Burke-Ernzerhof generalized gradient functional [74] with collinear spin polarization. The core configuration for the Fe PAW potential used in this paper was [Ar]3d<sup>7</sup>4s<sup>1</sup>. The plane-wave cutoff energy used in the calculations was 400 eV. Total energies were calculated using a  $\Gamma$ -centered Monkhorst-Pack mesh [75] of k-points in the Brillouin zone, with the k-mesh spacing of 0.16 Å<sup>-1</sup>, which corresponds to 14 × 14 × 14 k-point meshes for a two-atom BCC cell with a lattice parameter equal to 2.831 Å. To analyze the convergence of the DFT calculations, additional calculations have been performed for the k-mesh spacing of 0.11 Å<sup>-1</sup>, which corresponds to 20 × 20 × 20 k-point meshes for the same two-atom BCC cell. These calculations, which are more time consuming, do not offer substantial improvement of the accuracy with respect to those performed with the mesh spacing of 0.16 Å<sup>-1</sup>. The root-mean-square error (RMSE) between both datasets is 6.8 × 10<sup>-4</sup> eV, and the maximum error between them is 4 × 10<sup>-3</sup> eV. Additionally, no correlation has been found between the magnetic moment nor the volume with the energy differences. We conclude that the k-mesh spacing that refers to 14 × 14 × 14 k-point mesh for a two-atom BCC

cell is accurate enough to represent the energies in the dataset considered.

The database, which was used for the fitting of potential, consisted of DFT results performed when deforming two-atom structures with the positions of the atoms in a vertex and in the center of a rectangular cuboid, which corresponds to the relative positions (0,0,0) and (0.5,0.5,0.5) of the cubic cell considered, and different  $c/a$  and  $b/a$  ratios and volumes, where  $a$ ,  $b$ , and  $c$  are the three lattice magnitudes of the corresponding body-centered orthorhombic structure. Each DFT calculation was performed with a fixed shape and volume. Eight different values of volume  $V$  were considered from 9.25 to 12.75 Å<sup>3</sup>/atom with an interval equal to 0.5 Å<sup>3</sup>/atom. For each volume, 15 different values of  $c/a$  and  $b/a$  ratios were considered, namely: 0.7, 0.8, 0.9, 0.95, 1, 1.05, 1.1, 1.207, 1.3140, 1.3640,  $\sqrt{2}$ , 1.4640, 1.5140, 1.6, and 1.7. To not repeat calculations for structures, which are equal from the symmetry point of view, we used an assumption that the  $b/a$  ratio is bigger or equal to the  $c/a$  ratio. In total, 960 different structures were considered. For each of them, the calculations were performed for 10 different values of magnetic moment magnitudes  $M$  of atoms for the FM configuration, namely: 0, 0.5, 1, 1.5, 1.75, 2, 2.25, 2.5, 2.75, and 3.25  $\mu_B$  as well as for the magnetic moments optimized using self-consistent DFT calculations. The DFT calculations for AFM configurations with a constrained magnitude of magnetic moments were performed by adding a penalty contribution to the Hamiltonian, which is constructed in such a way that the total energy increases when there is a difference between the desired magnetic moment and the computed one. This penalty contribution could be avoided by using recent approaches based on the PAW method [76], although these are not currently implemented in VASP. The Wigner-Seitz radii in our calculations were chosen such that the overlap between the spheres is minimized. Since the computed magnitudes of magnetic moments in the AFM configurations were different to the desired ones, the total energies for the desired magnitudes of magnetic moments were interpolated from the computed values and corresponded then to the same magnetic moment magnitudes (0, 0.5, 1, 1.5, 1.75, 2, 2.25, 2.5, 2.75, and 3.25  $\mu_B$ ) as in the FM configuration.

This has produced 18 240 different ( $\langle c/a, b/a \rangle$ ,  $V$ ,  $M$ ) configurations, divided into 960 NM, 8640 FM, and 8640 AFM configurations. With this database structure, we cover a wide range of possible deformations of the  $\langle a, b, c \rangle$  cubic lattice, where the two most relevant cubic structures are included in the cases  $\langle c/a = 1, b/a = 1 \rangle$  for BCC and  $\langle c/a = 1, b/a = \sqrt{2} \rangle$  for FCC. A visualization of the calculations performed can be seen in Fig. 1 for both FM [Figs. 1(a)–1(c)] and AFM [in Figs. 1(d) and 1(e)] configurations, where the local ground state behavior for each lattice is displayed as a function of the  $c/a$  ratio (for the case  $b/a = 1$ ) and the atomic volume. Figure 1(c) shows some representatives cases, with  $c/a = 0.8, 1, 1.2, \sqrt{2}$ , and 1.6, for the energy (blue lines) in FM magnetic configuration, including the magnetic moment magnitude (orange lines) at which the local ground state is reached. Figure 1(f) shows the corresponding analysis in the AFM configuration also for the cases with  $c/a = 0.8, 1, 1.2, \sqrt{2}$ , and 1.6. In these figures, the configuration with minimum energy corresponds to FM BCC (at  $b/a = 1$ ). Additionally,

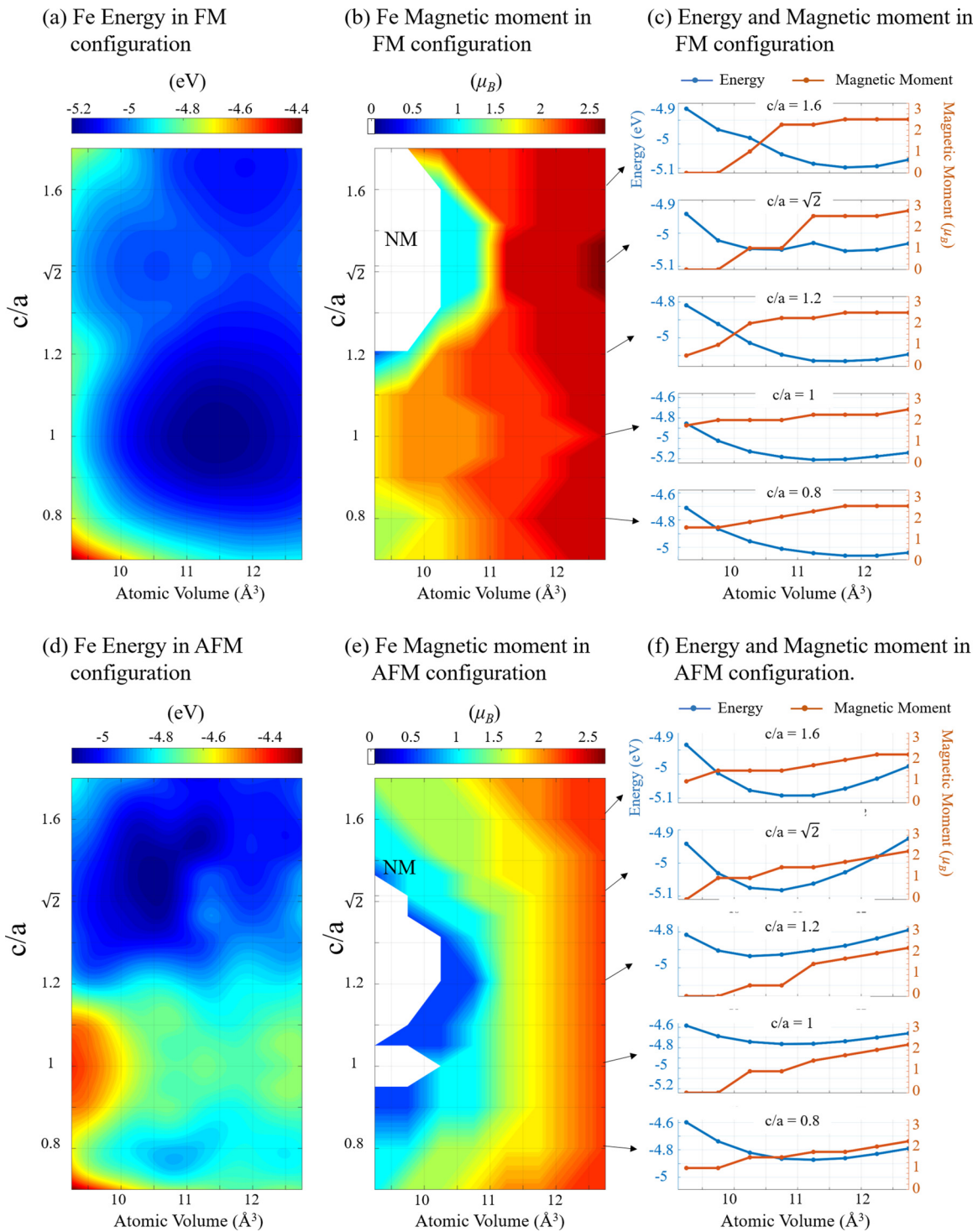


FIG. 1. (a) Ground state energy calculated by density functional theory (DFT) for ferromagnetic (FM) configuration and (b) corresponding magnetic moment, both as a function of atomic volume and  $c/a$  (with  $b/a = 1$ ). The corresponding curves for the energy and magnetic moments are displayed in (c) on representative cases of  $c/a$  ratio ( $c/a = 0.8, 1, 1.2, \sqrt{2}$ , and  $1.6$ ), where the blue lines represent the energy in FM configuration and the orange lines the corresponding magnetic moment. (d) Ground state energy calculated by DFT for antiferromagnetic (AFM) configuration and (e) corresponding magnetic moment, both as a function of atomic volume and  $c/a$  (with  $b/a = 1$ ). The corresponding curves for the energy and magnetic moments are displayed in (f) on representative cases of  $c/a$  ratio ( $c/a = 0.8, 1, 1.2, \sqrt{2}$ , and  $1.6$ ), where the blue lines represent the energy in AFM configuration and the orange lines the corresponding magnetic moment. NM stands for nonmagnetic.

the figure shows the regions where the NM configuration provides the local ground state [indicated as NM in Figs. 1(b) and 1(e)], which occurs for low atomic volumes and  $c/a$  ratios in the range of 1.2–1.7 for the FM case (around the FCC lattice), while the AFM case covers both BCC and FCC (with  $c/a$  ratios between 0.9 and 1.5). Next to these regions, low-spin (LS) magnetic configuration is observed covering a reasonable large variation of  $c/a$  ratios and atomic volumes. These can be observed in light and dark blue colors in both Figs. 1(b) and 1(e) (corresponding to  $\sim 0.25$ – $1 \mu_B$ ). The FCC crystal lattice shows therefore two minima in its ground state when varying the volume in the FM configuration, one at the LS state and another in the high-spin (HS) state. The minimum of these two minima occurs nevertheless in the HS state. It is worth noting that the magnetic moment of the LS is  $\sim 1 \mu_B$ , while a dramatic increase occurs for the HS state, where the values of the magnetic moment at the ground state vary between 2 and  $3 \mu_B$ , as observed in Fig. 1(c). Similarly, the AFM configuration shows also a LS state nearby the NM regions [Fig. 1(e)] with values of the magnetic moment even lower ( $\sim 0.5 \mu_B$ ). Nevertheless, this does not produce a two minima profile in the ground state energy, as occurs in the FM configuration. This can be seen in Sec. II of the Supplemental Material [77] which contains deeper insight into the behavior of the DFT calculations for other  $\langle c/a, b/a \rangle$  ratios for both magnetic configurations along with the corresponding magnetic behavior in some specific cases.

#### IV. DEVELOPMENT OF THE MIP FOR MAGNETIC Fe

##### A. Validation of the GUES

The proposed GUES in Eq. (5) must be examined before its use to describe the energy generated from DFT in a more general way. From the DFT binding energy calculated data ( $E_{\text{DFT}}$ ), the values of the potential parameters  $E_g^i(\rho, \mathbf{M})$ ,  $V_g^i(\rho, \mathbf{M})$ , and  $K_g^i(\rho, \mathbf{M})$  from Eq.(5) are fitted for each crystal structure and magnitude of the magnetic moment. In the database employed, the atomic coordinates are fixed for each structure, and these structures can be described via the  $\langle b/a, c/a \rangle$  ratios. Therefore, in this section, the variable corresponding to the relative interatomic distances per unit volume  $\rho$  will be expressed by means of  $\langle b/a, c/a \rangle$ .

As an initial illustrative case, the BCC and FCC crystal lattices are first considered in their respective NM and local ground state from the database. These correspond to  $M = 2.25 \mu_B$  (for BCC) and  $M = 2.5 \mu_B$  (for FCC) in the FM configuration, and  $M = 1 \mu_B$  (for BCC) and  $M = 1.5 \mu_B$  (for FCC) in the AFM configuration. The results can be seen in Fig. 2(a), where the DFT calculated data for these cases is displayed. The GUES is plotted with a solid line using the fitted values for  $E_g^i(\rho, \mathbf{M})$ ,  $V_g^i(\rho, \mathbf{M})$ , and  $K_g^i(\rho, \mathbf{M})$ , and their values are indicated in the figure legend. The GUES captures the energy variation by means of the volume for each of the cases. These DFT calculated energies have their counterpart values on the function  $F(V^*)$  of Eq. (1), at scaling by  $E_g^i(\rho, \mathbf{M})$  and Eq. (2). Their behavior can be seen in Fig. 2(b) showing a perfect fitting with  $F(V^*)$ .

This analysis can be extended to all DFT calculated energies and compare the results in a single plot using the scaled

energy value to  $F(V^*)$  for each point. The 18 240 different energies calculated are displayed in Fig. 2(c). Without exception, every  $\langle \langle b/a, c/a \rangle, M \rangle$  configuration varies its energy as a function of the volume, obeying the GUES in Eq. (5) for both magnetic configurations. Note that, for each  $\langle \langle b/a, c/a \rangle, M \rangle$  configuration, a different value for  $E_g^i(\rho, \mathbf{M})$ ,  $V_g^i(\rho, \mathbf{M})$ , and  $K_g^i(\rho, \mathbf{M})$  is found. In this figure, we have added the GUES corresponding calculation by using the Wigner-Seitz radius, as proposed initially in the UES, to be compared with the GUES prediction by using the volume. The GUES in Eq. (1) is plotted (shifted to facilitate the visualization) along with the calculated energies by the GUES (both with Wigner-Seitz radius and volume). Finally, the prediction of the energy, by using Eq. (5) and the corresponding fitted GUES parameters values for each  $\langle \langle b/a, c/a \rangle, M \rangle$  configuration, can be seen in Fig. 2(d) compared with the DFT calculated energies, showing an excellent fitting. For comparison purposes, the GUES using the Wigner-Seitz radius instead of the volume is also added. The results obtained show that both approaches provide a similar energy calculation.

The RMSE considering the 18 240 computed energies (at different crystal configurations, volumes, and magnetic configurations and moments) is  $3.9 \times 10^{-3}$  eV if the volume is used in the GUES, while the RMSE is  $1.3 \times 10^{-3}$  eV if the Wigner-Seitz radius is employed. Even though the Wigner-Seitz radius seems to provide a lower error, the difference is not significant, while the advantages of using the volume in the formulation incline the selection toward the volume. With this choice, the bulk modulus (it is explained below) is directly related to the GUES parameters, and the equation of motion permits us to include volume variations easily. We conclude that the proposed GUES can be used to describe the energy variation with respect to the volume for the DFT data in FM and AFM iron.

Based on these results, and as a concluding remark in this section, it is worth noting that the bulk modulus at the local ground state  $B_g^i(\rho, \mathbf{M})$  can be easily derived from the GUES and related to the potential parameters  $E_g^i(\rho, \mathbf{M})$ ,  $V_g^i(\rho, \mathbf{M})$ , and  $K_g^i(\rho, \mathbf{M})$ . By using Eq. (5) in the definition of bulk modulus as expressed in the following equation:

$$P(V) = -\frac{dE(V)}{dV} \quad \text{and} \quad B(V) = -V \frac{dP(V)}{dV}, \quad (10)$$

where  $P$  is the pressure, the evaluation of the expression obtained at the local ground state volume provides the local ground state bulk modulus:

$$\begin{aligned} B_g^i(\rho, \mathbf{M}) &= V \left\{ \frac{E_g^i(V, \rho, \mathbf{M})}{K_g^i(\rho, \mathbf{M})^2} \right. \\ &\quad \left. - 2 \frac{E_g^i(\rho, \mathbf{M}) \exp\left[-\frac{V-V_g^i(\rho, \mathbf{M})}{K_g^i(\rho, \mathbf{M})}\right]}{K_g^i(\rho, \mathbf{M})^2} \right\} \Bigg|_{V=V_g^i(\rho)} \\ &= -\frac{E_g^i(\rho, \mathbf{M}) V_g^i(\rho, \mathbf{M})}{K_g^i(\rho, \mathbf{M})^2}. \end{aligned} \quad (11)$$

Therefore, the energy of a solid can be then calculated at any volume by knowing the local ground state energy



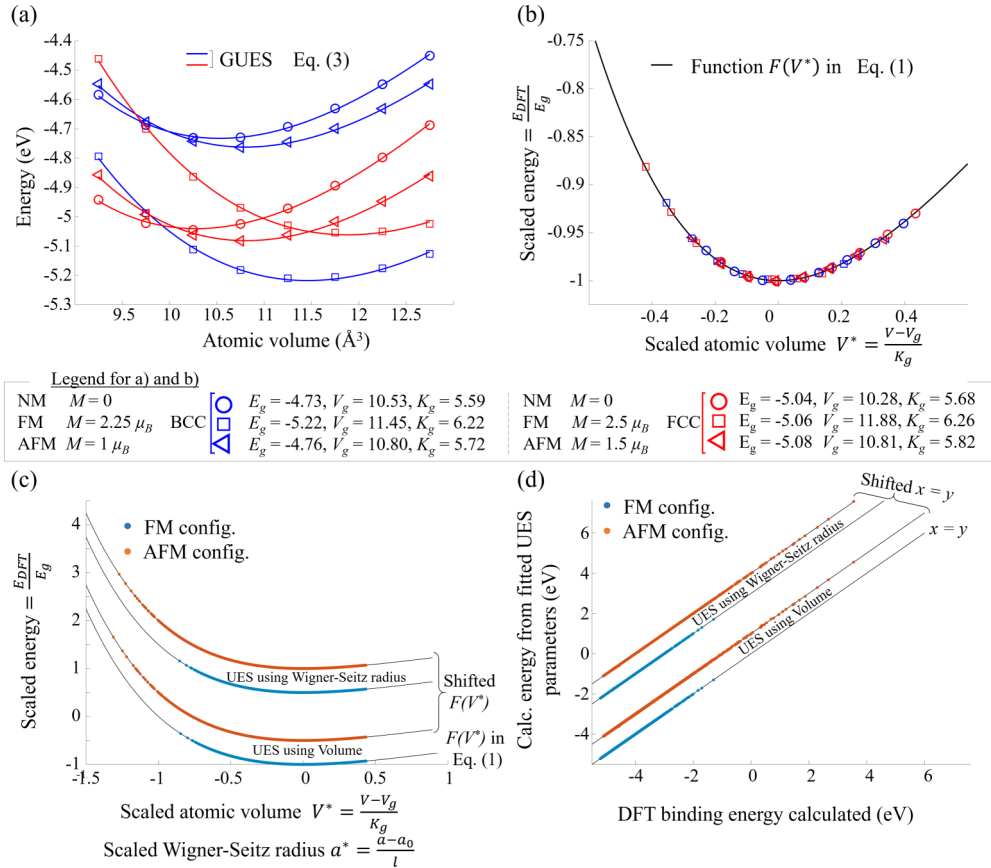


FIG. 2. (a) Energy variation with respect to the volume for the illustrative cases body-centered cubic (BCC) and face-centered cubic (FCC) crystal structures at different magnetic moments for the ferromagnetic (FM) and antiferromagnetic (AFM) configurations and corresponding energy function [Eq. (5)] at employing the fitted  $E_g^i(\rho, \mathbf{M})$  (in units of eV),  $V_g^i(\rho, \mathbf{M})$  and  $K_g^i(\rho, \mathbf{M})$  (both in units of  $\text{\AA}^3$ ) for each case. (b) Corresponding scaled energy vs function  $F(V^*)$  of Eq. (1). (c) Scaled energy vs function  $F(V^*)$  of Eq. (1) for all 18 240 density functional theory (DFT) calculated energies for FM and AFM cases. (d) Comparison between the 18 240 DFT calculated energies and the corresponding predicted energy using Eq. (5).

$E_0^i(\rho, \mathbf{M})$ , its corresponding volume  $V_0^i(\rho, \mathbf{M})$ , and bulk modulus  $B_0^i(\rho, \mathbf{M})$ .

### B. Analysis of the $E_g^i(\rho, \mathbf{M})$ , $V_g^i(\rho, \mathbf{M})$ , and $K_g^i(\rho, \mathbf{M})$ parameters

Once the validity of the GUES has been checked, the existence of a set of parameters  $E_g^i(\rho, \mathbf{M})$ ,  $V_g^i(\rho, \mathbf{M})$ , and  $K_g^i(\rho, \mathbf{M})$  that describes the energy of the system for each lattice and magnetic moment is proved. Now these parameters must be examined and related to the expressions in Eqs. (6) and (7) so that they are fully explained.

The calculations without magnetic contributions ( $M=0$ ) are firstly analyzed. This allows the analysis of the  $E_0^i(\rho)$ ,  $V_0^i(\rho)$ , and  $K_0^i(\rho)$  in Eq. (7). In the scope of the crystal configurations considered, all atoms are identical for a certain  $\langle b/a, c/a \rangle$  lattice, and consequently, they will have the same relative distances  $\rho_{ij}$ . Therefore,  $E_0^i(\rho)$ ,  $V_0^i(\rho)$ , and  $K_0^i(\rho)$  will have the same value for all atoms  $i$  in the lattice, and they can be analyzed as a function of  $\langle b/a, c/a \rangle$ . In this context,  $\rho$  represents  $\langle b/a, c/a \rangle$  and allows considering the energy  $E_0^i(b/a, c/a) \equiv E_0^i(\rho)$ , volume  $V_0^i(b/a, c/a) \equiv V_0^i(\rho)$ , and scaled volume  $K_0^i(b/a, c/a) \equiv K_0^i(\rho)$  as functional forms of  $\langle b/a, c/a \rangle$ . Nevertheless, for the sake of clarity and to keep

a homogeneous notation within this paper, we will keep the notation  $\rho$  to describe the interatomic distance dependence of the functions. Similarly, in the DFT database simulations, for each simulation, all atoms have the same magnitude of the magnetic moment. Therefore, in this section, we will denote  $M = M_i = M_j$  ( $j = 1, \dots, N$  with  $j \neq i$ ).

The fitted values of  $E_0^i(\rho)$ ,  $V_0^i(\rho)$ , and  $K_0^i(\rho)$  from DFT after numerical optimization at each lattice are displayed in Fig. 3. This figure shows a surprising result since the behaviors of  $E_0^i(\rho)$ ,  $V_0^i(\rho)$ , and  $K_0^i(\rho)$  are almost identical with minor differences, which arise from the numerical fitting. The ground state energy, its equilibrium volume, and corresponding volume scale correlate linearly. When modifying the crystal lattice, the change in local ground state energy follows an equivalent change in equilibrium volume and scaling volume. This result is of paramount importance since it suggests that there is a common and unique function generated by the atomic positions and its coordinates from which a direct behavior of the energy, volume, and scaling volume can be derived. Importantly, this motivates the definition of the term  $\omega_0(\rho_{ij})$  proposed in Eq. (7) which is now fully justified. The evaluation of  $\omega_0(\rho_{ij})$  for different lattices will make possible the calculation of  $E_0^i(\rho)$ ,  $V_0^i(\rho)$ , and  $K_0^i(\rho)$  and, therefore, the prediction of the energy variation with respect to the volume

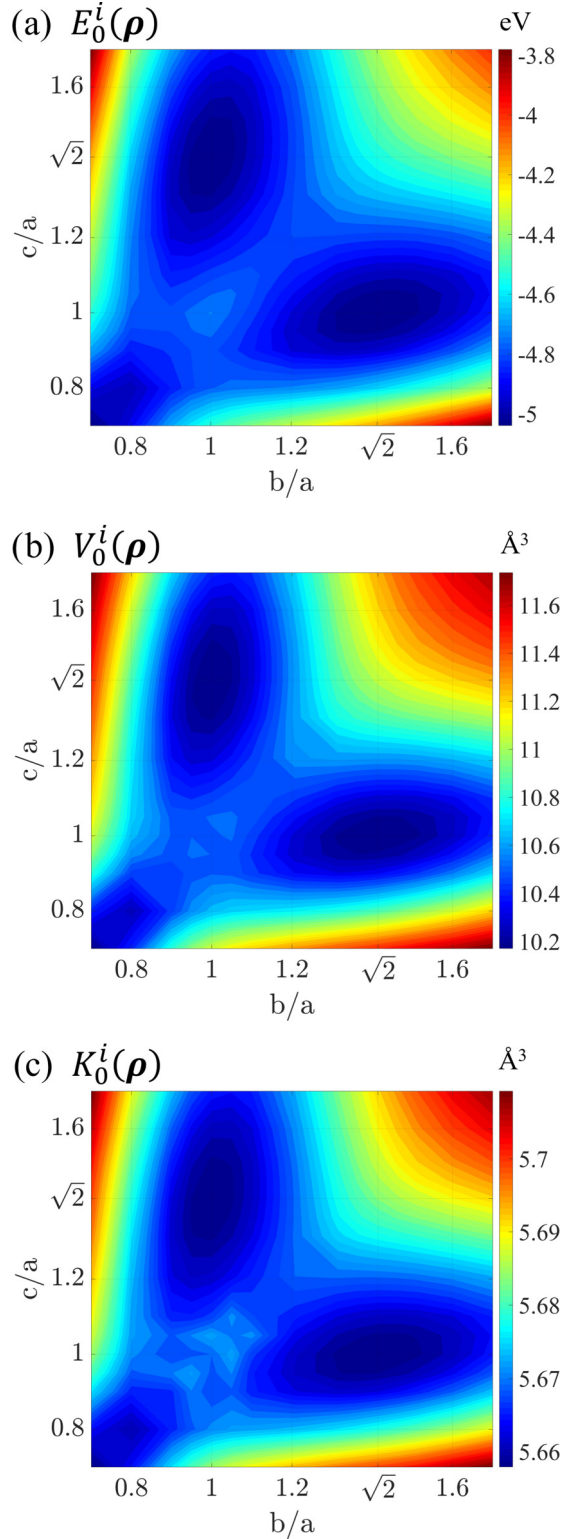


FIG. 3. Behavior of the parameters (a)  $E_0^i(\rho)$ , (b)  $V_0^i(\rho)$ , and (c)  $K_0^i(\rho)$  as functions of  $c/a$  and  $b/a$ .

using Eq. (5) for NM configurations. The definition of this function will be shown in Sec. IV C.

The behavior of the parameters  $E_g^i(\rho, \mathbf{M})$ ,  $V_g^i(\rho, \mathbf{M})$ , and  $K_g^i(\rho, \mathbf{M})$  with  $M \neq 0$  is now considered for both FM and AFM configurations. Like in the previous case

of  $E_0^i(\rho)$ ,  $V_0^i(\rho)$ , and  $K_0^i(\rho)$ , all atoms in a certain lattice ( $\langle b/a, c/a \rangle, M$ ) with the same magnetic configuration are indistinguishable, which makes  $M_i = M_j$ , where the subscript  $j \neq i$  represents all neighbor atoms of atom  $i$ . This permits the simplification of Eq. (6) into the following expression, which is only valid if all atoms have the same magnetic configuration and moment magnitude:

$$\begin{aligned}
 E_g^i(\rho, \mathbf{M}) &= E_0^i(\rho) + \Phi_E(M_i) + \sum_{j \neq i} \omega_M(\rho_{ij}) \sum_{j \neq i} \Psi_E(M_i, M_i) \\
 V_g^i(\rho, \mathbf{M}) &= V_0^i(\rho) + \Phi_V(M_i) + \sum_{j \neq i} \omega_M(\rho_{ij}) \sum_{j \neq i} \Psi_V(M_i, M_i) \\
 K_g^i(\rho, \mathbf{M}) &= K_0^i(\rho) + \Phi_K(M_i) + \sum_{j \neq i} \omega_M(\rho_{ij}) \sum_{j \neq i} \Psi_K(M_i, M_i).
 \end{aligned} \tag{12}$$

Note that the magnetically dependent functions  $\Psi$  depend in this expression only on  $M_i$ . This allows the analysis of the  $\omega_M(\rho_{ij})$  function isolated from  $\Psi$ , which will show a certain value for each of the  $b/a$  and  $c/a$  ratios, irrespective of the magnitude of the magnetic moment of the lattice. Similarly, the magnetically dependent functions  $\Psi$  can be analyzed irrespective of the lattice and the  $b/a$  and  $c/a$  ratios. The intention of this simplification is to provide the tool for analyzing both  $\omega_M$  and  $\Psi$  functions separately, always with the focus on using Eq. (6) for MD simulations.

Firstly, the numerically fitted  $E_g^i(\rho, \mathbf{M})$ ,  $V_g^i(\rho, \mathbf{M})$ , and  $K_g^i(\rho, \mathbf{M})$  using Eq. (5) from DFT are analyzed by means of the magnetic moment. Their variation with  $M$  can be seen in Fig. 4, where the colors displayed for different lines fit to the  $E_0^i(\rho)$ ,  $V_0^i(\rho)$ , and  $K_0^i(\rho)$  colors, respectively, as shown in Fig. 3.

From the figure, each crystal lattice  $\langle b/a, c/a \rangle$  behaves differently with respect to the magnetic moment, although they have similarities. In the case of  $E_g^i(\rho, \mathbf{M})$ , all lattices have a minimum value at magnetic moments in the range of  $2-3 \mu_B$  for both magnetic configurations, while  $V_g^i(\rho, \mathbf{M})$  increases monotonically with the magnetic moment. On the other hand,  $K_g^i(\rho, \mathbf{M})$  displays a very different behavior for the FM and AFM configurations.

In any case, their behavior, far from being random or chaotic, follows clear functional forms. Such mathematical expressions are unknown, but the fitted data can be used to approximate the functions by means of polynomials in the form of a Taylor expansion series. The following expressions are considered:

$$\begin{aligned}
 E_g^i(\rho, \mathbf{M}) &= E_0^i(\rho) + E_2^i(\rho)M^2 + E_4^i(\rho)M^4 \\
 &\quad + E_6^i(\rho)M^6 + O(M^8) \\
 V_g^i(\rho, \mathbf{M}) &= V_0^i(\rho) + V_2^i(\rho)M^2 + V_4^i(\rho)M^4 \\
 &\quad + V_6^i(\rho)M^6 + O(M^8) \\
 K_g^i(\rho, \mathbf{M}) &= K_0^i(\rho) + K_2^i(\rho)M^2 + K_4^i(\rho)M^4 \\
 &\quad + K_6^i(\rho)M^6 + O(M^8),
 \end{aligned} \tag{13}$$

where additional terms  $E_n^i(\rho)M^n$ ,  $V_n^i(\rho)M^n$ , and  $K_n^i(\rho)M^n$ , with  $n = 8, 10, 12, \dots$  can be added for a more accurate fitting of the curves shown in Fig. 4.

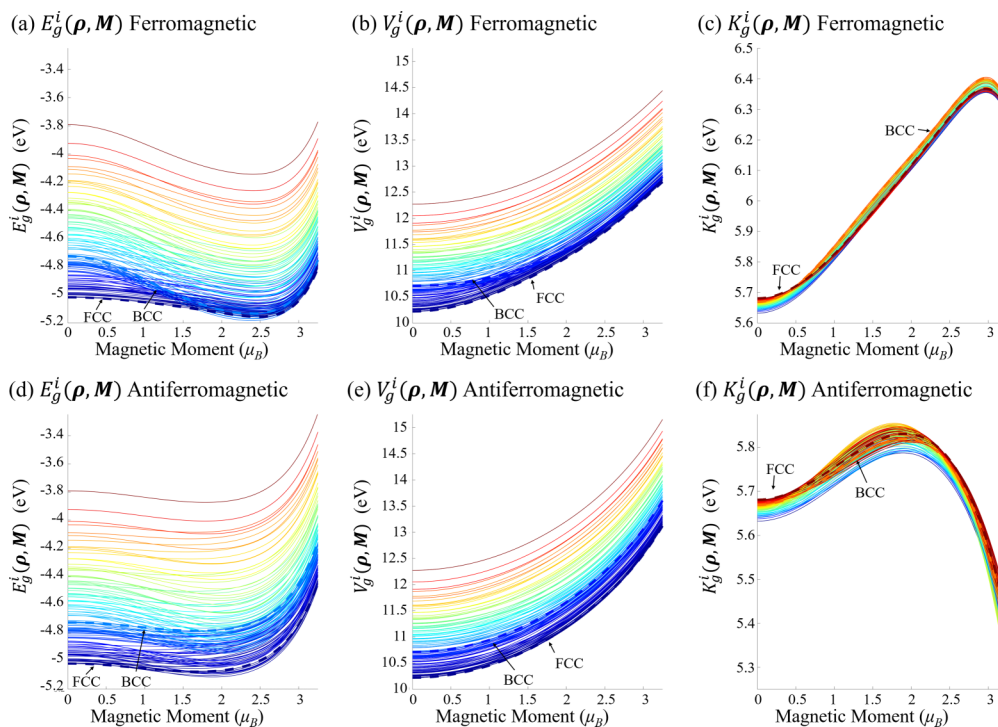


FIG. 4. Evolution with respect to the magnitude of the magnetic moment  $M$  of fitted values of (a)  $E_g^i(\rho, \mathbf{M})$  ferromagnetic (FM), (b)  $V_g^i(\rho, \mathbf{M})$  FM, (c)  $K_g^i(\rho, \mathbf{M})$  FM, (d)  $E_g^i(\rho, \mathbf{M})$  antiferromagnetic (AFM), (e)  $V_g^i(\rho, \mathbf{M})$  AFM, and (f)  $K_g^i(\rho, \mathbf{M})$  AFM. The colors correspond to the  $E_0^i(\rho)$ ,  $V_0^i(\rho)$ , and  $K_0^i(\rho)$  contour values, respectively, as shown in Fig. 3. The face-centered cubic (FCC) and body-centered cubic (BCC) corresponding curves are marked and indicated in each figure.

The reason behind the selection of polynomials with even exponents is because the mathematical expression of  $E_g^i(\rho, \mathbf{M})$ ,  $V_g^i(\rho, \mathbf{M})$ , and  $K_g^i(\rho, \mathbf{M})$  must be even functions to fulfill the Ginzburg-Landau approximation [51], which describes the energy dependence of the magnetic moment as an even polynomial. For a description of the relationship between the GUES and the Ginzburg-Landau approximation, see Sec. I in the Supplemental Material [77], where the behavior of both the FM and AFM cases is presented for different polynomial orders. The conclusion is that, only in certain cases (mostly close to BCC FM), order 4 is sufficient to describe the energy variation by means of the magnetic moment, as proposed by the Ginzburg-Landau approximation. Most  $\langle b/a, c/a \rangle$  crystal lattices need from the higher order even polynomials, and importantly, this applies to both FM and AFM configurations. The first consequence of this analysis is that the AFM behavior is not described by odd and even polynomials, and only even polynomials are needed. The second consequence is that a common formulation can be proposed for both magnetic configurations to cover all possible lattices.

The procedure to build the polynomials of Eq. (13) is simple and involves the least square method to fit the  $E_n^i(\rho)$ ,  $V_n^i(\rho)$ , and  $K_n^i(\rho)$  terms ( $n = 2, 4, 6, 8, \dots$ ) to the curves displayed in Fig. 4 corresponding to the numerically fitted  $E_g^i(\rho, \mathbf{M})$ ,  $V_g^i(\rho, \mathbf{M})$ , and  $K_g^i(\rho, \mathbf{M})$ . The results are shown in Fig. 5 for the FM configuration and Fig. 6 for the AFM configuration, where the parameters are displayed as a function of the  $\langle b/a, c/a \rangle$  ratios.

Like in the case of  $E_0^i(\rho)$ ,  $V_0^i(\rho)$ , and  $K_0^i(\rho)$ , there is an unexpected similar behavior between all  $E_n^i(\rho)$ ,  $V_n^i(\rho)$ , and  $K_n^i(\rho)$  parameters ( $n = 2, 4, 6, \dots$ ). They behave indeed different to the  $E_0^i(\rho)$ ,  $V_0^i(\rho)$ , and  $K_0^i(\rho)$  parameters, but a common shape can be seen for the  $E_n^i(\rho)$ ,  $V_n^i(\rho)$ , and  $K_n^i(\rho)$  in the FM configuration, as well as a common shape for the corresponding parameters in the AFM configuration, with small variations attributed to the fitting inaccuracies, around the BCC structure and in the scaling parameters  $K_n^i(\rho)$ . Extreme values occur for the BCC case ( $b/a = 1, c/a = 1$ ) and for the FCC case ( $b/a = 1, c/a = \sqrt{2}$ ) (which for the symmetry of  $\langle a, b, c \rangle$  cell parameters, they are equivalent to  $\langle b/a = \sqrt{2}, c/a = 1 \rangle$  and  $\langle b/a = \frac{\sqrt{2}}{2}, c/a = \frac{\sqrt{2}}{2} \rangle$ ). The sequence is nevertheless inverted as the order increases. In other words, the maximum for  $E_2^i(\rho)$  is minimum in  $E_4^i(\rho)$ , and maximum again in  $E_6^i(\rho)$ , and inversely. The same effect happens for  $V_2^i(\rho)$ ,  $V_4^i(\rho)$ , and  $V_6^i(\rho)$  as well as for  $K_2^i(\rho)$ ,  $K_4^i(\rho)$ , and  $K_6^i(\rho)$ . This behavior resembles the relationships of the coefficients of a Taylor expansion series, suggesting that closed expressions for  $E_g^i(\rho, \mathbf{M})$ ,  $V_g^i(\rho, \mathbf{M})$ , and  $K_g^i(\rho, \mathbf{M})$  functions exist. Although these closed expressions remain unknown, this opens the possibility to reduce dramatically the complexity of predicting such functions (and thus the energy of cubic structures at any magnetic moment) since, in the same way as proposed for the NM contribution, a unique distance-dependent function  $\omega_M^{\text{FM}}(\rho_{ij})$  for the FM configuration and a unique distance-dependent function  $\omega_M^{\text{AFM}}(\rho_{ij})$  for the AFM configuration can be proposed to reproduce all  $E_n^i(\rho)$ ,  $V_n^i(\rho)$ ,

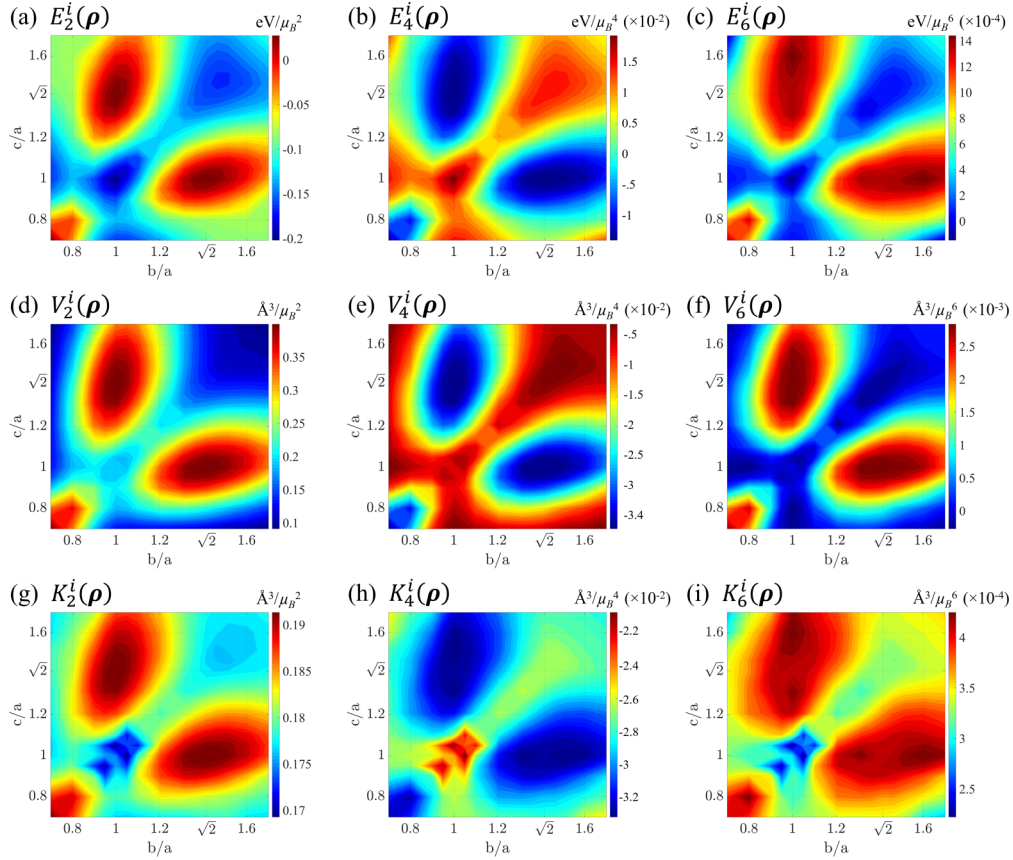


FIG. 5. Behavior of the fitted parameters (a)  $E_2^i(\rho)$ , (b)  $E_4^i(\rho)$ , (c)  $E_6^i(\rho)$ , (d)  $V_2^i(\rho)$ , (e)  $V_4^i(\rho)$ , (f)  $V_6^i(\rho)$ , (g)  $K_2^i(\rho)$ , (h)  $K_4^i(\rho)$ , and (i)  $K_6^i(\rho)$  with respect to  $\langle b/a, c/a \rangle$  for the ferromagnetic configuration.

and  $K_n^i(\rho)$  behaviors. For the sake of clarity and to propose a unified notation, we will use  $\omega_M(\rho_{ij})$  to denote correspondingly  $\omega_M^{\text{FM}}(\rho_{ij})$  or  $\omega_M^{\text{AFM}}(\rho_{ij})$ . The proposed expressions for  $E_n^i(\rho, M)$ ,  $V_n^i(\rho, M)$ , and  $K_n^i(\rho, M)$  then read

$$\left\{ \begin{array}{l} E_n^i(\rho) = \varepsilon_{n,0} + \varepsilon_{n,1} \sum_{j \neq i} \omega_M(\rho_{ij}) \\ V_n^i(\rho) = \nu_{n,0} + \nu_{n,1} \sum_{j \neq i} \omega_M(\rho_{ij}) \\ K_n^i(\rho) = \kappa_{2,0} + \kappa_{2,1} \sum_{j \neq i} \omega_M(\rho_{ij}) \end{array} \right\} \text{ for } n = 2, 4, 6, \dots, \quad (14)$$

where the parameters  $\varepsilon_{n,1}$  ( $n = 2, 4, 6, 8, \dots$ ) alternate signs to fit with the behavior observed in Fig. 5 as well as the  $\nu_{n,1}$  and  $\kappa_{n,1}$  [except in the case of AFM  $K_n^i(\rho)$ ].

The consequence of this observed behavior is of paramount importance and motivates the existence of the functions  $\Phi_E$ ,  $\Phi_V$ ,  $\Phi_K$ ,  $\Psi_E$ ,  $\Psi_V$ , and  $\Psi_K$  as they have been proposed in Eq. (6). When applying Eq. (14) into Eq. (13), the terms can be easily rearranged and form the following expressions:

$$\begin{aligned} \Phi_E(M) &= \varepsilon_{2,0}M^2 + \varepsilon_{4,0}M^4 + \varepsilon_{6,0}M^6 + \dots \\ \Phi_V(M) &= \nu_{2,0}M^2 + \nu_{4,0}M^4 + \nu_{6,0}M^6 + \dots \\ \Phi_K(M) &= \kappa_{2,0}M^2 + \kappa_{4,0}M^4 + \kappa_{6,0}M^6 + \dots \\ \Psi_E(M) &= \varepsilon_{2,1}M^2 + \varepsilon_{4,1}M^4 + \varepsilon_{6,1}M^6 + \dots \\ \Psi_V(M) &= \nu_{2,1}M^2 + \nu_{4,1}M^4 + \nu_{6,1}M^6 + \dots \end{aligned}$$

$$\psi_K(M) = \kappa_{2,1}M^2 + \kappa_{4,1}M^4 + \kappa_{6,1}M^6 + \dots \quad (15)$$

The values of  $\varepsilon_{n,0}$ ,  $\varepsilon_{n,1}$ ,  $\nu_{n,0}$ ,  $\nu_{n,1}$ ,  $\kappa_{n,0}$ , and  $\kappa_{n,1}$  ( $n = 2, 4, 6, 8, \dots$ ) fitted from the procedure described allow the approximation of the functions  $\Phi_E$ ,  $\Phi_V$ ,  $\Phi_K$ ,  $\psi_E$ ,  $\psi_V$ , and  $\psi_K$ . These must be understood as unknown functional forms of the magnetic moments, which are approximated via the numerical evaluation of their Taylor expansion coefficients. The prediction of the DFT calculated energy by using this approximation is presented in the following section, where these magnetically dependent functions are introduced.

### C. Fitted distance and magnetically dependent functions

To display the common functions that describe  $E_0^i(\rho, \mathbf{M})$ ,  $V_0^i(\rho, \mathbf{M})$ , and  $K_0^i(\rho, \mathbf{M})$  and  $E_g^i(\rho, \mathbf{M})$ ,  $V_g^i(\rho, \mathbf{M})$ , and  $K_g^i(\rho, \mathbf{M})$  for both FM and AFM configurations, we define the following functions, which depend only on the crystal lattice via  $\langle b/a, c/a \rangle$ :

$$\begin{aligned} \Omega_0(\rho) &= \sum_{j \neq i} \omega_0(\rho_{ij}) \\ \Omega_M^{\text{FM}}(\rho) &= \sum_{j \neq i} \omega_M^{\text{FM}}(\rho_{ij}) \\ \Omega_M^{\text{AFM}}(\rho) &= \sum_{j \neq i} \omega_M^{\text{AFM}}(\rho_{ij}), \end{aligned} \quad (16)$$

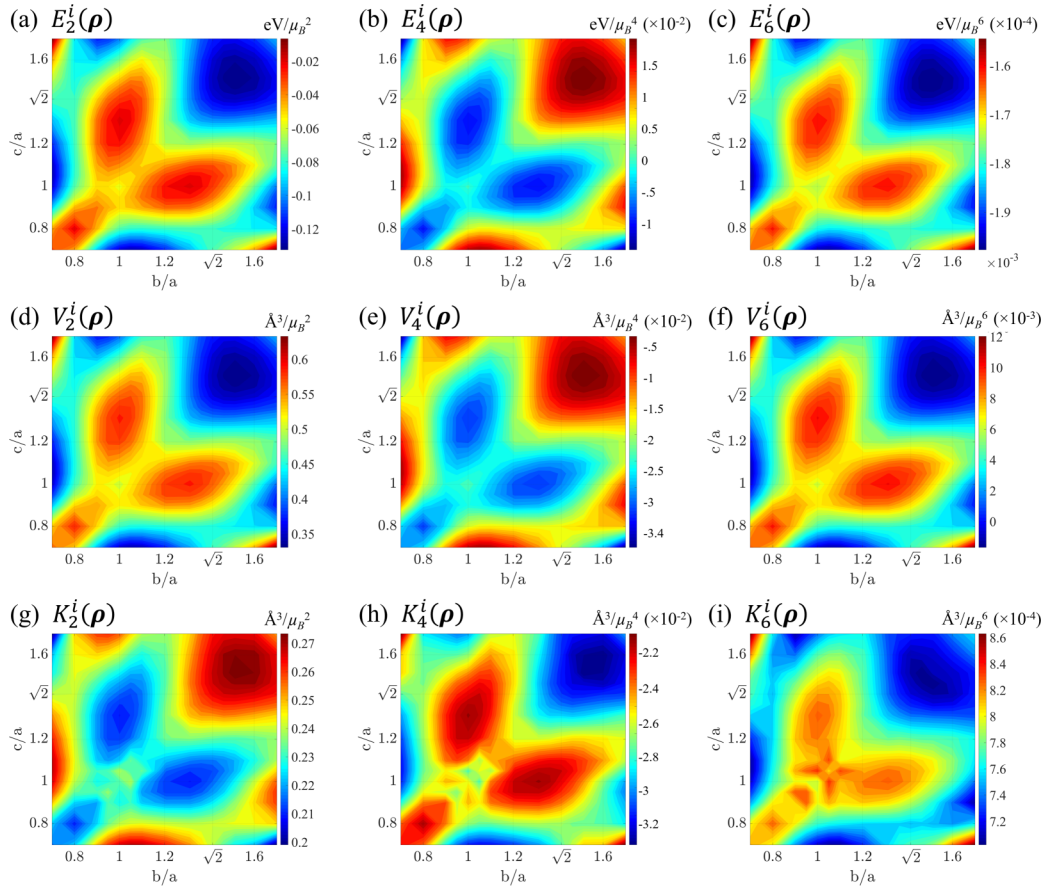


FIG. 6. Behavior of the fitted parameters (a)  $E_2^i(\rho)$ , (b)  $E_4^i(\rho)$ , (c)  $E_6^i(\rho)$ , (d)  $V_2^i(\rho)$ , (e)  $V_4^i(\rho)$ , (f)  $V_6^i(\rho)$ , (g)  $K_2^i(\rho)$ , (h)  $K_4^i(\rho)$ , and (i)  $K_6^i(\rho)$  with respect to  $\langle b/a, c/a \rangle$  for the antiferromagnetic configuration.

where the notation  $\rho$  represents the sequence of interatomic distances for a certain  $\langle b/a, c/a \rangle$  lattice.

The fitted parameters for Eqs. (7) and (15) can be seen in Table I for both magnetic configurations, where order 8 of the series expansion has been selected since it provides a good fitting to the DFT calculated energy.

The proposed  $\Omega_0(\rho)$ ,  $\Omega_M^{\text{FM}}(\rho)$ , and  $\Omega_M^{\text{AFM}}(\rho)$  functions can be seen in Figs. 7(a)–7(c), respectively. The functions are selected to display the same behavior seen in Figs. 3, 5, and 6, respectively. It is worth noting that the range of values selected for these functions is arbitrary since the parameters  $\varepsilon_{0,0}$ ,  $\varepsilon_{0,1}$ ,  $\nu_{0,0}$ ,  $\nu_{0,1}$ ,  $\kappa_{0,0}$ , and  $\kappa_{0,1}$  will be selected consequently to obtain  $E_0^i(\rho)$ ,  $V_0^i(\rho)$ , and  $K_0^i(\rho)$ . Similarly, the parameters  $\varepsilon_{n,0}$ ,  $\varepsilon_{n,1}$ ,  $\nu_{n,0}$ ,  $\nu_{n,1}$ ,  $\kappa_{n,0}$ , and  $\kappa_{n,1}$  for  $n = 2, 4, 6, 8, \dots$  are fitted to provide  $\Phi_E(M_i)$ ,  $\Phi_V(M_i)$ ,  $\Phi_K(M_i)$ ,  $\Psi_E(M_i, M_j)$ ,  $\Psi_V(M_i, M_j)$ , and  $\Psi_K(M_i, M_j)$  functions. These magnetically dependent functions can be seen in Fig. 7(d) for the FM configuration and Fig. 7(e) for the AFM configuration. In these figures, a double y axis is used to display the magnetic functions, where the  $\Phi_V(M_i)$ ,  $\Phi_K(M_i)$ ,  $\Psi_V(M_i, M_j)$ , and  $\Psi_K(M_i, M_j)$  functions correspond to the left axis, while  $\Phi_E(M_i)$  and  $\Psi_E(M_i, M_j)$  correspond to the right axis. As it happens with the distance-dependent  $\omega_M^{\text{FM}}$  and  $\omega_M^{\text{AFM}}$  functions, which provide  $\Omega_M^{\text{FM}}$  and  $\Omega_M^{\text{AFM}}$ , the magnetic functions are different in the FM and AFM configuration. It is worth noting that the (arbitrary) ranges of the functions  $\Omega_M^{\text{FM}}$  and  $\Omega_M^{\text{AFM}}$  are selected to have similar  $\Phi$  and  $\Psi$  functions.

Finally, the use of all these functions in Eq. (5) and (6) provides the energy predictions, which are compared with the DFT corresponding ones in Fig. 7(f), where the RMSE of the fitting is  $2 \times 10^{-2}$  eV for the FM case and  $9 \times 10^{-2}$  eV for the AFM case. The errors are indeed larger than the errors obtained when numerically fitting the  $E_g$ ,  $V_g$ , and  $K_g$  parameters, as shown in Fig. 2(d). The difference is especially larger in the AFM data. On one hand, this can be attributed to the larger complexity of the magnetic configuration, where spins alternate signs. On the other hand, the computation of the energies at the magnetic moment magnitudes (0, 0.5, 1, 1.5, 1.75, 2, 2.25, 2.5, 2.75, and 3.25  $\mu_B$ ) in DFT are approximated. This was described in Sec. III, where a constrained magnitude of the magnetic moments was performed by adding a penalty contribution to the Hamiltonian, providing magnitude moments in the AFM configuration close but not exactly to the targeted ones. The interpolation used is needed to calculate the variation of the  $E_g$ ,  $V_g$ , and  $K_g$  parameters as a function of the magnetic moment in a consistent manner as it was done in the FM case. This procedure may affect the DFT calculations and the corresponding distance- and magnetically dependent functions obtained.

Despite these results, we conclude that the predictions are well in line with the DFT calculations and that common functions exist to provide accurate predictions of the FM and AFM configurations by means of the proposed interatomic potential formulation.

TABLE I. Fitted parameters of Eqs. (7) and (15) for the FM and AFM configurations.

	Function	Parameter	Value	Parameter	Value	Parameter	Value
FM	Eq. (7)	$\varepsilon_{0,0}$	$-5.055$ (eV)	$\nu_{0,0}$	$10.171$ ( $\text{\AA}^3$ )	$\kappa_{0,0}$	$5.677$ ( $\text{\AA}^3$ )
		$\varepsilon_{0,1}$	$3.386 \times 10^{-1}$ (eV)	$\nu_{0,1}$	$5.562 \times 10^{-1}$ ( $\text{\AA}^3$ )	$\kappa_{0,1}$	$-8.842 \times 10^{-3}$ ( $\text{\AA}^3$ )
	$\Phi_E, \Phi_V, \Phi_K$ Eq. (15)	$\varepsilon_{2,0}$	$3.168 \times 10^{-2}$ (eV/ $\mu_B^2$ )	$\nu_{2,0}$	$4.569 \times 10^{-1}$ ( $\text{\AA}^3/\mu_B^2$ )	$\kappa_{2,0}$	$1.705 \times 10^{-1}$ ( $\text{\AA}^3/\mu_B^2$ )
		$\varepsilon_{4,0}$	$-7.339 \times 10^{-3}$ (eV/ $\mu_B^4$ )	$\nu_{4,0}$	$-6.619 \times 10^{-2}$ ( $\text{\AA}^3/\mu_B^4$ )	$\kappa_{4,0}$	$-2.838 \times 10^{-2}$ ( $\text{\AA}^3/\mu_B^4$ )
		$\varepsilon_{6,0}$	$-1.574 \times 10^{-4}$ (eV/ $\mu_B^6$ )	$\nu_{6,0}$	$7.881 \times 10^{-3}$ ( $\text{\AA}^3/\mu_B^6$ )	$\kappa_{6,0}$	$3.829 \times 10^{-3}$ ( $\text{\AA}^3/\mu_B^6$ )
		$\varepsilon_{8,0}$	$7.965 \times 10^{-5}$ (eV/ $\mu_B^8$ )	$\nu_{8,0}$	$-3.270 \times 10^{-4}$ ( $\text{\AA}^3/\mu_B^8$ )	$\kappa_{8,0}$	$-2.044 \times 10^{-4}$ ( $\text{\AA}^3/\mu_B^8$ )
	$\Psi_E, \Psi_V, \Psi_K$ Eq. (15)	$\varepsilon_{2,1}$	$-2.762 \times 10^{-1}$ (eV/ $\mu_B^2$ )	$\nu_{2,1}$	$-3.982 \times 10^{-1}$ ( $\text{\AA}^3/\mu_B^2$ )	$\kappa_{2,1}$	$3.836 \times 10^{-2}$ ( $\text{\AA}^3/\mu_B^2$ )
		$\varepsilon_{4,1}$	$5.438 \times 10^{-2}$ (eV/ $\mu_B^4$ )	$\nu_{4,1}$	$1.026 \times 10^{-1}$ ( $\text{\AA}^3/\mu_B^4$ )	$\kappa_{4,1}$	$-7.062 \times 10^{-3}$ ( $\text{\AA}^3/\mu_B^4$ )
		$\varepsilon_{6,1}$	$-4.478 \times 10^{-3}$ (eV/ $\mu_B^6$ )	$\nu_{6,1}$	$-1.203 \times 10^{-2}$ ( $\text{\AA}^3/\mu_B^6$ )	$\kappa_{6,1}$	$4.287 \times 10^{-4}$ ( $\text{\AA}^3/\mu_B^6$ )
		$\varepsilon_{8,1}$	$1.367 \times 10^{-4}$ (eV/ $\mu_B^8$ )	$\nu_{8,1}$	$5.016 \times 10^{-4}$ ( $\text{\AA}^3/\mu_B^8$ )	$\kappa_{8,1}$	$-6.796 \times 10^{-6}$ ( $\text{\AA}^3/\mu_B^8$ )
AFM	$\Phi_E, \Phi_V, \Phi_K$ Eq. (15)	$\varepsilon_{2,0}$	$-9.419 \times 10^{-3}$ (eV/ $\mu_B^2$ )	$\nu_{2,0}$	$2.763 \times 10^{-1}$ ( $\text{\AA}^3/\mu_B^2$ )	$\kappa_{2,0}$	$6.545 \times 10^{-2}$ ( $\text{\AA}^3/\mu_B^2$ )
		$\varepsilon_{4,0}$	$9.212 \times 10^{-3}$ (eV/ $\mu_B^4$ )	$\nu_{4,0}$	$-3.935 \times 10^{-3}$ ( $\text{\AA}^3/\mu_B^4$ )	$\kappa_{4,0}$	$-4.924 \times 10^{-3}$ ( $\text{\AA}^3/\mu_B^4$ )
		$\varepsilon_{6,0}$	$-9.630 \times 10^{-4}$ (eV/ $\mu_B^6$ )	$\nu_{6,0}$	$4.055 \times 10^{-4}$ ( $\text{\AA}^3/\mu_B^6$ )	$\kappa_{6,0}$	$-6.294 \times 10^{-4}$ ( $\text{\AA}^3/\mu_B^6$ )
		$\varepsilon_{8,0}$	$6.852 \times 10^{-5}$ (eV/ $\mu_B^8$ )	$\nu_{8,0}$	$5.321 \times 10^{-6}$ ( $\text{\AA}^3/\mu_B^8$ )	$\kappa_{8,0}$	$3.826 \times 10^{-5}$ ( $\text{\AA}^3/\mu_B^8$ )
	$\Psi_E, \Psi_V, \Psi_K$ Eq. (15)	$\varepsilon_{2,1}$	$-1.905 \times 10^{-1}$ (eV/ $\mu_B^2$ )	$\nu_{2,1}$	$-1.824 \times 10^{-1}$ ( $\text{\AA}^3/\mu_B^2$ )	$\kappa_{2,1}$	$1.248 \times 10^{-1}$ ( $\text{\AA}^3/\mu_B^2$ )
		$\varepsilon_{4,1}$	$1.457 \times 10^{-2}$ (eV/ $\mu_B^4$ )	$\nu_{4,1}$	$1.532 \times 10^{-2}$ ( $\text{\AA}^3/\mu_B^4$ )	$\kappa_{4,1}$	$-5.217 \times 10^{-2}$ ( $\text{\AA}^3/\mu_B^4$ )
		$\varepsilon_{6,1}$	$-6.354 \times 10^{-4}$ (eV/ $\mu_B^6$ )	$\nu_{6,1}$	$-2.616 \times 10^{-4}$ ( $\text{\AA}^3/\mu_B^6$ )	$\kappa_{6,1}$	$6.791 \times 10^{-3}$ ( $\text{\AA}^3/\mu_B^6$ )
		$\varepsilon_{8,1}$	$6.161 \times 10^{-5}$ (eV/ $\mu_B^8$ )	$\nu_{8,1}$	$3.162 \times 10^{-7}$ ( $\text{\AA}^3/\mu_B^8$ )	$\kappa_{8,1}$	$-3.333 \times 10^{-4}$ ( $\text{\AA}^3/\mu_B^8$ )

#### D. MIP definition

In this subsection, the definition of the MIP for FM configuration is presented. It is worth noting that the GUES, as introduced in Sec. II, is the proposed formalism to describe the energy of a system and has been validated in Sec. IV C,

where the  $\omega_0$  and  $\omega_M$  distance-dependent functions are introduced in Eq. (16) but not defined yet. Only the  $\Omega_0$  and  $\Omega_M$  functions in Eq. (16) (displayed in Fig. 7 for the FM and AFM configurations) are defined so far, which are a consequence of evaluating  $\omega_0$  and  $\omega_M$  in a certain lattice with ideal positions

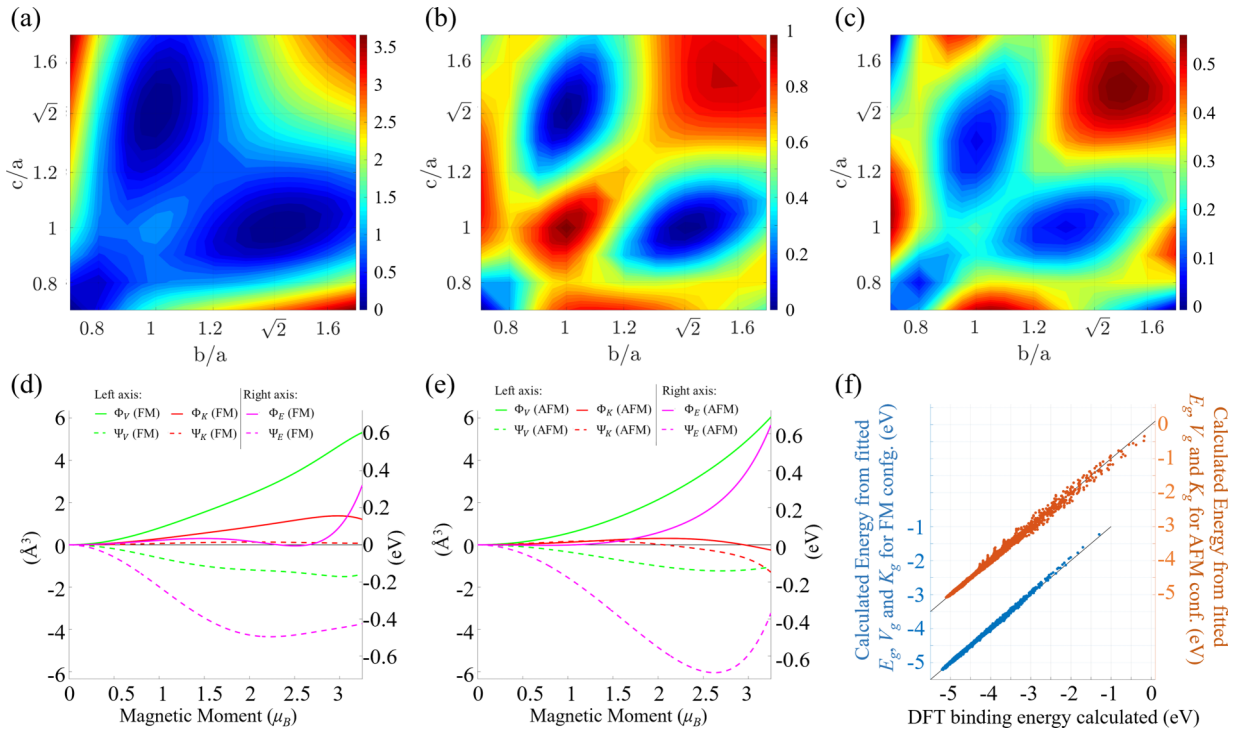


FIG. 7. (a) Functional form of  $\Omega_0$ , (b) functional form of  $\Omega_M^{\text{FM}}$ , (c) functional form of  $\Omega_M^{\text{AFM}}$  as a function of  $(\frac{b}{a}, \frac{c}{a})$ , (d)  $\Phi_E(M)$ ,  $\Psi_E(M)$ ,  $\Phi_V(M)$ ,  $\Phi_K(M)$ , and  $\Psi_K(M)$  for the ferromagnetic (FM) configuration, (e)  $\Phi_E(M)$ ,  $\Psi_E(M)$ ,  $\Phi_V(M)$ ,  $\Psi_V(M)$ ,  $\Phi_K(M)$ , and  $\Psi_K(M)$  for the antiferromagnetic (AFM) configuration, and (f) corresponding energy calculated by using  $\omega_0(\rho)$ ,  $\omega_M(\rho)$ ,  $\Phi_E(\mathbf{M})$ ,  $\Psi_E(\mathbf{M})$ ,  $\Phi_V(\mathbf{M})$ ,  $\Psi_V(\mathbf{M})$ ,  $\Phi_K(\mathbf{M})$ , and  $\Psi_K(\mathbf{M})$  into Eqs. (5), (7), and (12) for both FM and AFM configurations.

(and therefore constant for all atoms in such lattice). For this reason, the  $\Omega_0$  and  $\Omega_M$  functions are unusable to perform MD simulations, where the atoms move from ideal positions.

Consequently, atom-atom distance-dependent interaction functions  $\omega_0$  and  $\omega_M$  must be defined explicitly. Also important to note, the  $\Omega_M$  has been seen to be different for the FM and AFM configurations. Correspondingly,  $\omega_M$  is also different for each magnetic configuration. For this reason, in this paper, we have focused only on describing the FM case, which represents the most relevant magnetic configuration in Fe.

Concerning the development of the FM potential, special attention must be paid to the definition of the magnetically dependent functions. The  $\Phi_E(M_i)$ ,  $\Phi_V(M_i)$ , and  $\Phi_K(M_i)$  func-

tions correspond to the Landau-Ginsburg formulation for the magnetic self-energy terms, while  $\Psi_E(M_i, M_j)$ ,  $\Psi_V(M_i, M_j)$ , and  $\Psi_K(M_i, M_j)$ , scaled by  $\omega_M(\rho_{ij})$ , represent the lattice magnetic configuration described by the intersite Heisenberg magnetic interaction parameters. These latter ones involved the magnetic moment of two different atoms  $M_i$  and  $M_j$  by multiplication of their magnitudes  $M_i \times M_j$ . In this paper, and to be consistent with both the even polynomials introduced in Eq. (13) for the  $\Psi$  functions and the Heisenberg-Landau Hamiltonian, the equivalent polynomial expansion can also be applied for magnetic moment quantity  $\sqrt{M_i M_j}$ . Therefore, the magnetic functions, expressed as a function of the magnetic moments of two different atoms  $M_i$  and  $M_j$ , are now approximated by

$$\begin{aligned}
 \Phi_E(M_i) &= \varepsilon_{2,0} M_i^2 + \varepsilon_{4,0} M_i^4 + \varepsilon_{6,0} M_i^6 + \varepsilon_{8,0} M_i^8 \\
 \Phi_V(M_i) &= \nu_{2,0} M_i^2 + \nu_{4,0} M_i^4 + \nu_{6,0} M_i^6 + \nu_{8,0} M_i^8 \\
 \Phi_K(M_i) &= \kappa_{2,0} M_i^2 + \kappa_{4,0} M_i^4 + \kappa_{6,0} M_i^6 + \kappa_{8,0} M_i^8 \\
 \Psi_E(M_i, M_j) &= \varepsilon_{2,1} M_i M_j + \varepsilon_{4,1} (M_i M_j)^2 + \varepsilon_{6,1} (M_i M_j)^3 + \varepsilon_{8,1} (M_i M_j)^4 \\
 \Psi_V(M_i, M_j) &= \nu_{2,1} M_i M_j + \nu_{4,1} (M_i M_j)^2 + \nu_{6,1} (M_i M_j)^3 + \nu_{8,1} (M_i M_j)^4 \\
 \Psi_K(M_i, M_j) &= \kappa_{2,1} M_i M_j + \kappa_{4,1} (M_i M_j)^2 + \kappa_{6,1} (M_i M_j)^3 + \kappa_{8,1} (M_i M_j)^4.
 \end{aligned} \tag{17}$$

It is worth noting that order 8 in the polynomial expressions of  $M_i$ , and equivalently order 4 for  $M_i \times M_j$ , has been seen to provide a good prediction of the magnetic influence in the FM configuration using the proposed formulation. Higher polynomials do not offer significant improvements in accuracy, while order 6 (equivalent order 3 for  $M_i \times M_j$ ) or smaller fails at predicting the energy behavior correctly. This is consistent with the Heisenberg-Landau Hamiltonian formulation proposed in Ref. [28] concerning the Landau coefficients for the magnetic self-energy terms, which shows also order 8 in its polynomial expansion but extends the polynomial order defined in the interlattice-site Heisenberg magnetic interaction parameters, which was defined to be a function only of  $M_i \times M_j$ .

Once the expressions for the FM interatomic potential are defined, the fitted expressions are presented hereinafter. Attractive-repulsive pairwise functions are considered for  $\omega_0(\rho_{ij})$  and  $\omega_M(\rho_{ij})$ . Most known interatomic potentials use this type of function since they capture the nature of atomic forces. Simple forms like the classical Lennard-Jones potentials or Morse potential have close functions that describe independently the attractive and repulsive forces. On the other hand, the EAM methodology is based on density-dependent potentials derived from DFT, where the atom is assumed to be embedded in an electron cloud, originated by its surrounding atoms. The repulsive term is described by means of a pair potential on the distance between atoms, while the attractive term depends on a functional describing the energy of embedding an atom in the bulk density. EAM being consistent with the UES by Vinet *et al.* [56] and Rose *et al.* [55] used here to describe the energy-volume relationship [78,79], attractive-repulsive functions are used similarly to

describe the atom-atom distance interaction [80]. No simple closed functions have been found to describe these attractive-repulsive functions, and in this paper, a combination of several Gaussian functions have been employed to build a function capable of fitting all DFT data along the crystal structures considered. The selection of Gaussians is not arbitrary since they provide differentiability along with simplicity. A sum of several Gaussians,  $\sim 80$ , with their centers spaced 0.1 between  $\rho_{ij} = 0$  and 8, is used, with a standard deviation equal to 1, where their height is optimized to obtain  $\omega_0(\rho_{ij})$  and  $\omega_M(\rho_{ij})$ . The proposed functions of  $\omega_0(\rho_{ij})$  and  $\omega_M(\rho_{ij})$  have been fitting using a least squared method to approximate the  $\Omega_0$  and  $\Omega_M$  functions defined in Figs. 7(a) and 7(b), respectively. A visualization of the obtained functions is displayed in Fig. 8.

The magnetically dependent  $\Phi$  and  $\Psi$  functions have been refitted from those proposed in Fig. 7(c) to maximize the accuracy of the MIP once  $\omega_0(\rho_{ij})$  and  $\omega_M(\rho_{ij})$  are defined. The predicted  $\Omega_0$  and  $\Omega_M$  using the fitted  $\omega_0(\rho_{ij})$  and  $\omega_M(\rho_{ij})$  functions have minor differences with respect to the original  $\Omega_0$  and  $\Omega_M$  functions, and consequently, the magnetically dependent functions are very similar to those originally proposed. Their fitted behavior is displayed in Fig. 8(b), where the  $\Psi$  functions are expressed via the equivalent-combined magnetic moment  $M = \sqrt{M_i M_j}$ .

See Sec. III of the Supplemental Material [77] for the tabulated expressions for  $\omega_0(\rho_{ij})$  and  $\omega_M(\rho_{ij})$ ,  $\Phi_E(M_i)$ ,  $\Phi_V(M_i)$ ,  $\Phi_K(M_i)$ ,  $\Psi_E(M_i, M_j)$ ,  $\Psi_V(M_i, M_j)$ , and  $\Psi_K(M_i, M_j)$ . Note that the  $\Psi$  functions are tabulated via  $M = \sqrt{M_i M_j}$ . It is important to note that this potential has eight functions to be evaluated for each simulation step. This represents indeed a larger computational effort than other potentials proposed, such as the EAM, where only two functions are used, one

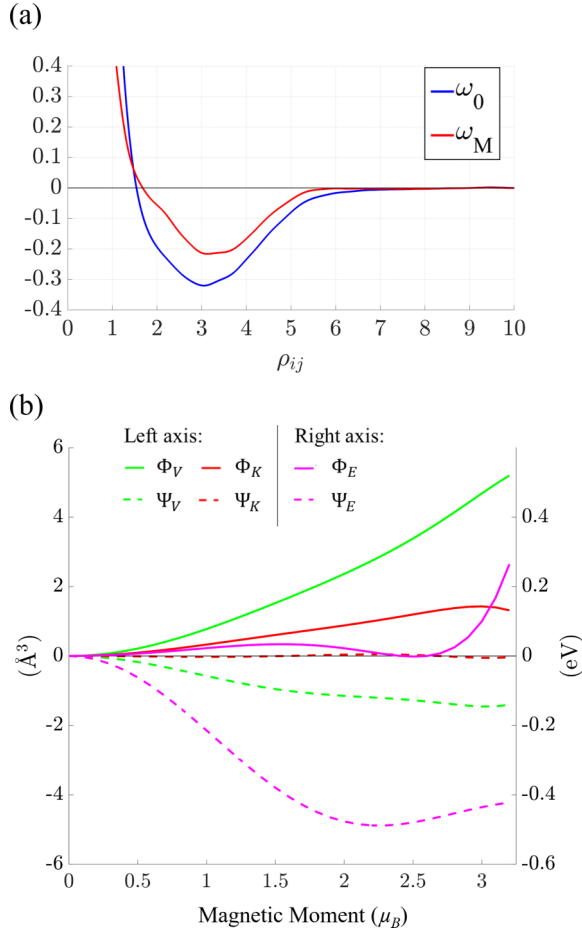


FIG. 8. Functions of the magnetic interatomic potential for the ferromagnetic Fe case, (a) distance-dependent functions  $\omega_0(\rho_{ij})$  and  $\omega_M(\rho_{ij})$  of Eqs. (6) and (7) and (b) magnetically dependent  $\Phi$  and  $\Psi$  functions of Eq. (6).

for the contribution to the electron charge density between two atoms and another corresponding to the pairwise potential. This difference is logically due to the incorporation of magnetism in the formulation since seven of the functions of the MIP are related to magnetism. Nevertheless, the MIP still allows for computational speed comparable with other interatomic potentials, being much lower than the DFT method.

Finally, the fitted parameters which defines  $E_0^i(\rho)$ ,  $V_0^i(\rho)$ ,  $K_0^i(\rho)$ ,  $E_g^i(\rho, \mathbf{M})$ ,  $V_g^i(\rho, \mathbf{M})$ , and  $K_g^i(\rho, \mathbf{M})$  as functions shown in Eqs. (7) and (17) are displayed in Table II:

## V. VALIDATION OF THE POTENTIAL AND ITS PREDICTABILITY

The performance of the GUES was validated in Sec. IV C, whereas now the fitted interatomic potential based on the GUES needs to be validated once the  $\omega_0$  and  $\omega_M$  have been explicitly proposed. The validation is performed in the database employed and computed by DFT, as described in Sec. III, which is also employed here to check the predictability of the MIP. It is important to note that the GUES is the proposed formalist that allows developing the MIP. In this regard, the GUES was validated once the  $E_g$ ,  $V_g$ , and  $K_g$  parameters were fitted, directly from DFT calculations. The  $\omega_0$  and  $\omega_M$  distance-dependent functions are not deducted from this fitting, and only the  $\Psi$  and  $\Phi$  magnetically dependent functions were defined. Therefore, once the  $\omega_0$  and  $\omega_M$  are proposed (and  $\Psi$  and  $\Phi$  refitted with minor differences to the ones used in the GUES), an initial analysis in the same database employed for the developing GUES is needed. Later in this section, the use of the MIP to analyze its predictability outside the limits of the DFT database is treated.

Starting from the validation of the MIP, the behavior of the fitted  $\omega_0(\rho_{ij})$  functions with respect to  $(b/a, c/a)$  can be seen in Fig. 9(a), showing a similar behavior with respect to the  $\Omega_0$  function in Fig. 7(a). The parameters to reproduce the behavior  $E_g^0(\rho)$ ,  $V_g^0(\rho)$ , and  $K_g^0(\rho)$  in Eq. (7), as shown in Fig. 3, are displayed in Table II. Similarly, the behavior of  $\omega_M(\rho_{ij})$  is shown in Fig. 9(b), where  $\Omega_M$  is calculated, also showing a similar behavior to  $\Omega_M$  proposed in Fig. 7. The value of the parameters to obtain  $E_n^i(\rho)$ ,  $V_n^i(\rho)$ , and  $K_n^i(\rho)$  ( $n = 2, 4, 6$ , and  $8$ ) in Eq. (14) are also displayed in Table II. These parameters are used to build the  $\Phi_E(M_i)$ ,  $\Phi_V(M_i)$ ,  $\Phi_K(M_i)$ ,  $\Psi_E(M_i, M_j)$ ,  $\Psi_V(M_i, M_j)$ , and  $\Psi_K(M_i, M_j)$  magnetic functions of Eq. (17) and displayed in Fig. 8(b).

The  $\omega_0(\rho_{ij})$  and  $\omega_M(\rho_{ij})$  functions can be considered to represent a short-range potential. To illustrate this and taking the case of iron in the BCC structure with the cell parameter at equilibrium  $a = 2.86 \text{ \AA}$ , the corresponding  $\rho_{ij}$  of the second nearest neighbor equals 2, which is interpreted as two atoms per unit cell. Similarly, the first, second, third, and fourth

TABLE II. Parameters for the functions  $E_0^i(\rho)$ ,  $V_0^i(\rho)$ ,  $K_0^i(\rho)$ ,  $E_g^i(\rho, \mathbf{M})$ ,  $V_g^i(\rho, \mathbf{M})$ , and  $K_g^i(\rho, \mathbf{M})$  defined in Eqs. (7) and (17).

Function	Parameter	Value	Parameter	Value	Parameter	Value
Eq. (7)	$\epsilon_{0,0}$	$-5.057 \text{ (eV)}$	$\nu_{0,0}$	$1.017 \text{ (\AA}^3\text{)}$	$\kappa_{0,0}$	$5.659 \text{ (\AA}^3\text{)}$
	$\epsilon_{0,1}$	$3.326 \times 10^{-1} \text{ (eV)}$	$\nu_{0,1}$	$5.460 \times 10^{-1} \text{ (\AA}^3\text{)}$	$\kappa_{0,1}$	$1.376 \times 10^{-2} \text{ (\AA}^3\text{)}$
	$\epsilon_{2,0}$	$2.819 \times 10^{-2} \text{ (eV}/\mu_B^2\text{)}$	$\nu_{2,0}$	$4.405 \times 10^{-1} \text{ (\AA}^3/\mu_B^2\text{)}$	$\kappa_{2,0}$	$1.978 \times 10^{-1} \text{ (\AA}^3/\mu_B^2\text{)}$
Eq. (17)	$\epsilon_{4,0}$	$-5.250 \times 10^{-3} \text{ (eV}/\mu_B^4\text{)}$	$\nu_{4,0}$	$-5.950 \times 10^{-2} \text{ (\AA}^3/\mu_B^4\text{)}$	$\kappa_{4,0}$	$-3.864 \times 10^{-2} \text{ (\AA}^3/\mu_B^4\text{)}$
	$\epsilon_{6,0}$	$-4.833 \times 10^{-4} \text{ (eV}/\mu_B^6\text{)}$	$\nu_{6,0}$	$6.954 \times 10^{-3} \text{ (\AA}^3/\mu_B^6\text{)}$	$\kappa_{6,0}$	$5.235 \times 10^{-3} \text{ (\AA}^3/\mu_B^6\text{)}$
	$\epsilon_{8,0}$	$9.505 \times 10^{-5} \text{ (eV}/\mu_B^8\text{)}$	$\nu_{8,0}$	$-2.855 \times 10^{-4} \text{ (\AA}^3/\mu_B^8\text{)}$	$\kappa_{8,0}$	$-2.672 \times 10^{-4} \text{ (\AA}^3/\mu_B^8\text{)}$
	$\epsilon_{2,1}$	$-2.585 \times 10^{-1} \text{ (eV}/\mu_B^2\text{)}$	$\nu_{2,1}$	$-3.706 \times 10^{-1} \text{ (\AA}^3/\mu_B^2\text{)}$	$\kappa_{2,1}$	$-2.762 \times 10^{-2} \text{ (\AA}^3/\mu_B^2\text{)}$
Eq. (17)	$\epsilon_{4,1}$	$4.736 \times 10^{-2} \text{ (eV}/\mu_B^4\text{)}$	$\nu_{4,1}$	$9.217 \times 10^{-2} \text{ (\AA}^3/\mu_B^4\text{)}$	$\kappa_{4,1}$	$1.744 \times 10^{-2} \text{ (\AA}^3/\mu_B^4\text{)}$
	$\epsilon_{6,1}$	$-3.505 \times 10^{-3} \text{ (eV}/\mu_B^6\text{)}$	$\nu_{6,1}$	$-1.061 \times 10^{-2} \text{ (\AA}^3/\mu_B^6\text{)}$	$\kappa_{6,1}$	$-2.910 \times 10^{-3} \text{ (\AA}^3/\mu_B^6\text{)}$
	$\epsilon_{8,1}$	$9.307 \times 10^{-5} \text{ (eV}/\mu_B^8\text{)}$	$\nu_{8,1}$	$4.387 \times 10^{-4} \text{ (\AA}^3/\mu_B^8\text{)}$	$\kappa_{8,1}$	$1.418 \times 10^{-4} \text{ (\AA}^3/\mu_B^8\text{)}$



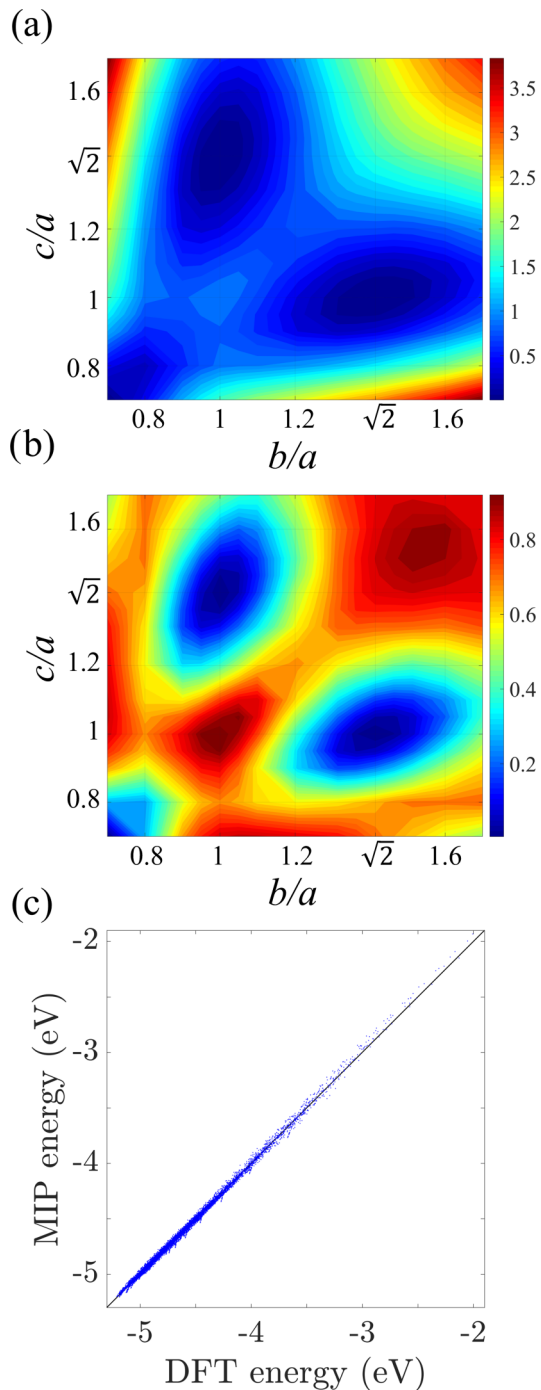


FIG. 9. (a) Obtained  $\Omega_0$  using the  $\omega_0(\rho)$  function as a function of  $\langle \frac{b}{a}, \frac{c}{a} \rangle$ . (b) Obtained  $\Omega_M$  using the  $\omega_M(\rho)$  function as a function of  $\langle \frac{b}{a}, \frac{c}{a} \rangle$ . (c) Comparison between the density functional theory (DFT) calculations and predicted energy by using the magnetic interatomic potential (MIP) in the 9600 energies calculated (960 nonmagnetic and 8640 ferromagnetic).

nearest atoms in the cited BCC structure corresponding to  $r_{ij} = 2.47, 2.86, 4.04,$  and  $4.74 \text{ \AA}$  take the values  $\rho_{ij} = 1.299, 2, 5.65,$  and  $9.12$ , respectively. Following the functions displayed in Fig. 8(a), this implies that the most relevant atoms correspond to the first, second, and third nearest neighbors. It is important to note that this result also applies to any cell

parameter of such a BCC structure. In other words, a constant cutoff interatomic distance cannot be considered since, for a BCC structure with a cell parameter of  $2.7 \text{ \AA}$  (as opposed to the previous example), its corresponding first, second, third, and fourth nearest atoms occur now at  $r_{ij} = 2.34, 2.7, 3.82,$  and  $4.47 \text{ \AA}$ , but the same values of  $\rho_{ij}$  apply as for the case with  $a = 2.86 \text{ \AA}$ . The cutoff, if applied to optimize the computational cost, is on the variable  $\rho_{ij}$  and not in the interatomic distance  $r$ .

With this potential, the corresponding energy calculation on the 9600 DFT energy points has now a RMSE of  $1.9 \times 10^{-2} \text{ eV}$ . The comparison between the DFT computed energies and those predicted by the MIP can be seen in Fig. 9(c), where a good fitting is observed. This proves that two distance-dependent functions and two magnetically dependent functions are needed to calculate  $E_g, V_g,$  and  $K_g$  for all crystal configurations and magnetic moments.

The cohesive energy, volume, and magnetic moment at the BCC ground state using the MIP correspond to  $-5.208 \text{ eV}, 11.659 \text{ \AA}^3/\text{atom},$  and  $2.39 \mu_B$ , respectively, while the DFT calculations predict  $-5.21 \text{ eV}, 11.35 \text{ \AA}^3/\text{atom},$  and  $2.199 \mu_B$  [29]. For comparison purposes, the experimental observation of the BCC ground state is an equilibrium volume of  $11.692 \text{ \AA}^3/\text{atom}$  [81] and magnetic moment  $2.22 \mu_B$  [82], showing that the theoretical computations are correct.

From the energy predictions of both the DFT calculations and the MIP, a calculation of the minimum energy obtained for each  $(\langle b/a, c/a \rangle, V)$  configuration can be performed, selecting from the different  $M$  considered those most energetically favorable. For the case  $b/a = 1$ , the results can be seen in Figs. 10(a) and 10(b), where the MIP predictions of the energy and corresponding magnetic moment providing the ground state for each  $c/a$  and volume considered (with  $b/a = 1$ ) are displayed, respectively. In these figures, the regions where the minimum energy is reached without magnetic contribution are indicated with NM. These figures should be compared with Figs. 1(a) and 1(b), where a similar analysis is depicted from the DFT computed energies and magnetic moments. Despite the small differences obtained, the MIP successfully predicts the energy and corresponding magnetic state when varying  $c/a$  and  $V$ .

Along with the contour plots shown in Figs. 10(a) and 10(b), in Fig. 10(c), for some representative  $c/a$  cases ( $c/a = 0.8, 1, 1.2, \sqrt{2},$  and  $1.6$ ), energy curves (blue lines) and the corresponding magnetic moment variations (orange lines) are shown. This figure should be compared with Fig. 1(c), where the same analysis is carried out for the DFT computations. The results show a high degree of consistency of the MIP prediction in both energy and magnetic moment. We conclude that, in general, not only the energy is correctly calculated but also the magnetic moment which provides such energy. Importantly, the variation of the energy by means of the volume for the FCC crystal lattice [see Fig. 10(c) case  $c/a = \sqrt{2}$ ] shows two minima, a known result in FM iron [83] and shown also in Fig. 1(c) for the DFT prediction. In both simulations, the NM configuration occurs at low volumes, followed by a LS state as the volume increases, and finally, a HS state provides the second minimum. Nevertheless, it is worth noting that the minimum corresponding to low volumes occurs in DFT for

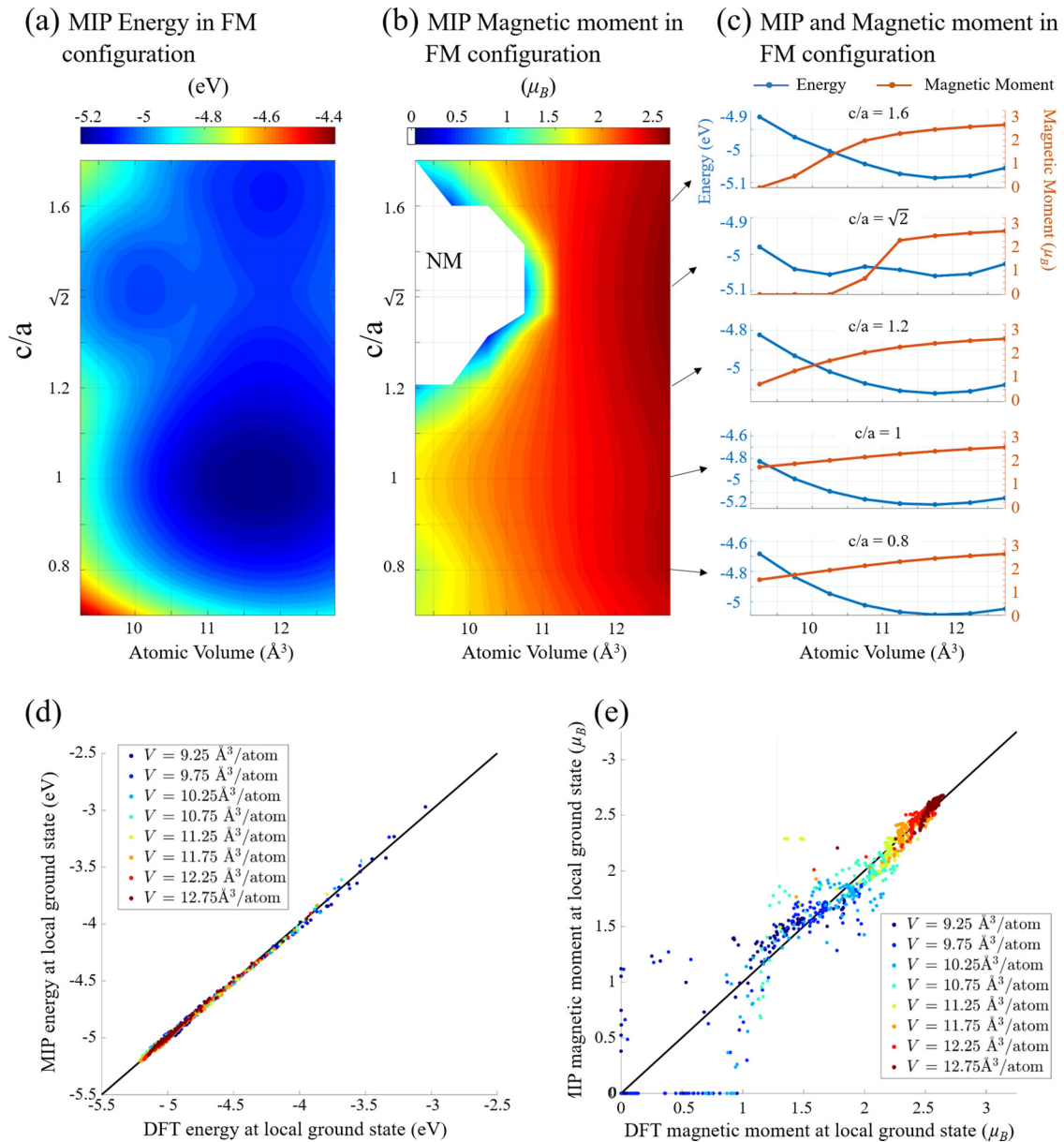


FIG. 10. (a) Ground state energy calculated by the magnetic interatomic potential (MIP) for ferromagnetic (FM) configuration and (b) corresponding magnetic moment, both as a function of atomic volume and  $c/a$  (with  $b/a = 1$ ). The corresponding curves for the energy and magnetic moments are displayed in (c) on representative cases of  $c/a$  ratio ( $c/a = 0.8, 1, 1.2, \sqrt{2},$  and  $1.6$ ), where the blue lines represent the energy in FM configuration and the orange lines the corresponding magnetic moment. (d) Comparison of the energies calculated by density functional theory (DFT) and the MIP at the local ground state for each  $((b/a, c/a), V)$  configuration and (e) corresponding comparison of the magnetic moments calculated by DFT and MIP at the local ground state for each  $((b/a, c/a), V)$  configuration.

the LS state, whereas the MIP predicts the NM configuration. However, the MIP energy prediction at the first minimum is  $-5.056$  eV, while the corresponding value of MIP energy at a LS state is  $-5.027$ , a variation  $<0.03$  eV. Additionally, the DFT energy at the first minimum is  $-5.048$ , very close to the DFT energy with a NM contribution which is  $-5.045$  and an energy difference of  $0.003$  eV. Even though the MIP fails at predicting that the first minimum occurs with a LS state, the energy differences in DFT and the MIP to obtain LS or NM configuration are significantly small, and although there is room for improvement, the general performance of the potential is good.

The calculation of the ground state is of paramount importance in the development of interatomic potentials since it provides the right configuration and energy of a system in equilibrium (or para-equilibrium) rather than the prediction of energies in different  $((b/a, c/a), V, M)$  configurations. Such configurations are considered very useful in the scope of development and fitting of the potential as well as to prove the generalization of the UES proposed but remain less important in the application of the MIP developed, as many of these configurations are never reached in a real system. Therefore, additionally to the analysis shown in Figs. 10(a)–10(c), the magnetic moment is optimized to obtain the minimum

energy for a given  $(\langle b/a, c/a \rangle, V)$ . This extends the preliminary comparison performed and provides the first test of the MIP predictability outside the energy calculations when fixing  $(\langle b/a, c/a \rangle, V, M)$ . Therefore, for each  $(\langle b/a, c/a \rangle, V)$ , both DFT and the MIP are used to calculate the corresponding local ground state, where the values of magnetic moments are not fixed but optimized. The results of the energies obtained are displayed in Fig. 10(d), where the points are depicted in different colors according to the volume considered. The MIP provides a RMSE = 0.025 eV compared with the DFT energies, where the larger errors, in the range of 0.07–0.09 eV, correspond to the extreme values of  $\langle b/a, c/a \rangle$  and lower atomic volumes. Figure 10(e) shows the corresponding optimized magnetic moment. The behavior of the MIP there is, in general, in agreement with the DFT calculations, where the MIP predictions show the NM configuration in lattices and DFT shows a LS state at low atomic volumes. This explains the issue explained above concerning the first minimum when fixing  $c/a = 1$  and  $c/a = \sqrt{2}$ , where DFT predicts a LS state and the MIP predicts a NM configuration. It is worth remembering that, even though the MIP predicted magnetic configuration differs from the DFT calculations at these low volumes, the energy is correctly calculated. For higher volumes, the MIP performance is good in both energy and magnetic moment.

#### A. Predictability of the potential

From the results in the previous section concerning the validation of the potential into the original database, we conclude that the calculation of the energy for the 9600 cubic deformed structures at different volumes and magnetic configurations provided an excellent fitting with respect to DFT calculations. Itself, this is already a good result since no other type of interatomic potential has been capable of predicting this large variety of crystal structures, magnetic moments, and volumes. It is nevertheless important to put to the test the MIP in other crystal structures, atomic configurations and parameters and compare the results to test its predictive capabilities.

Therefore, the intention of this section is to perform a series of validations on key situations not included in the database used for the fitting and test the applicability of the proposed potential. The number of tests to which a potential can be put is vast and could cover an immense and unmanageable piece of work. We have selected a few of them which, to our understanding, cover key properties. Firstly, elastic constants of magnetic  $\alpha$ -iron, simple parameters but of great relevance, as well as stresses in all the lattices and volumes of the database will be considered, as well as forces compared with *ab initio* MD (AIMD) simulations at different temperatures. Then the deformation of the BCC structure toward other lattices will be analyzed by means of transformation paths. Following that, the A15 and C15 crystal structures represent the simplest complex structures, where the magnetic moments are not constant along with their atoms. Increasing complexity, point defects in the way of vacancies and interstitial atoms (corresponding to dumbbell structures) cover the following steps, while the last step is the calculation of  $\gamma$  surfaces which are relevant for the mechanical behavior.

#### 1. Elastic constants

Elastic constants represent the first mandatory validation test for an interatomic potential. The calculation is made on the ground state configuration, magnetic  $\alpha$ -iron, where C11, C12, and C44 are constants. For the MIP calculation, small strain steps of 0.005% are used to analyze small deformations. For each step, the magnetic moment is optimized to obtain the corresponding ground state. The results are displayed in Table III, along with the bulk modulus, shear modulus, Young's modulus, and Poisson's ratio computed by the Voigt-Reuss-Hill method [84,85], and compared with experimental values from the literature as well as other DFT calculations, modified EAM (MEAM), linear machine learning (LML), and quadratic noise machine learning (QNML).

The results show that the C11, C12, and C44 constants are predicted, all with an error <15 GPa with respect to the DFT calculations in this paper. The corresponding bulk modulus is accurately predicted since this parameter is indirectly involved in the MIP formulation, as shown in Eq (11). Shear modulus, Young's modulus, and Poisson's ratio predictions lie in reasonable error limits, where the worst prediction occurs for Young's modulus, which is overestimated as compared with the DFT calculations in this paper. The comparison with experimental and other DFT calculations lies within reasonable limits. On the other hand, there is an overestimation, especially in the C11 and C12 cases, in all DFT calculations (both from literature and reported here), which is consequently inherited by the MIP, as can be observed in the data shown in Table III.

#### 2. Atomic stresses and forces in the lattice

The calculation of the atomic stresses on the lattices considered is now under investigation. Each of these lattices has nonzero forces acting on their respective atoms since only one crystal lattice corresponds to the  $\alpha$ -iron ground state. These forces are good indicators of the behavior of the MIP to predict the evolution of the system in a simulation. The atomic stresses in DFT and MIP approaches are calculated by computing the energy  $E$  when applying a strain  $\varepsilon_\alpha$  on each of the three spatial coordinates ( $\alpha = x, y, z$ ) and approximating the energy variation by means of a quartic polynomial, from which the first derivative permits the calculation of the atomic stresses in the lattice. The following equation is therefore used to account for the energy variation:

$$E = E_0 + \Gamma_1 \varepsilon_\alpha + \frac{1}{2} \Gamma_2 \varepsilon_\alpha^2 + \dots, \quad (18)$$

where the linear term  $\Gamma_1 = V \sigma_\alpha$  accounts for the total stress of the system,  $V$  is the atomic volume, and  $\sigma_\alpha$  corresponds to the atomic stress at straining over coordinates  $\alpha = x, y, z$ . The strain step considered for this calculation is 0.01% of the corresponding lattice parameter.

The comparison of the stresses between the DFT and MIP calculations can be seen in Fig. 11, showing a good fitting, where each color is associated with each of the three spatial coordinates. Some outliers can be observed, and the fitting of the larger stress values is slightly worse than the lower values. These larger errors correspond again to the extreme values of  $\langle b/a, c/a \rangle$ , which are the lattices least stable of all. The corresponding RSME is  $1.4 \text{ eV}/\text{\AA}^3$ ,

TABLE III. Comparison between the elastic constants from DFT and MIP in this paper and experimental values, MEAM, LML, QNML, and other DFT calculations. C11, C12, C44, bulk modulus, shear modulus and Young's modulus are expressed in GPa.

Approach	Experimental				MEAM		LML	QNML	DFT			MIP	
Ref.	[86]	[87]	[88]	[89]	[90]	[91]	[92]	[92]	[92]	[93]	[94]	(This paper)	(This paper)
C11	239.5	243.1	230	232	231.3	265.7	287.7	293.6	292.2	296.8	234.4	277.3	272.5
C12	135.9	138.1	135	136	134.6	127.5	148.5	144.0	144.3	142.06	119.1	151.9	159.7
C44	120.7	121.9	117	117	116.2	122.6	120.5	102.3	102.1	106.03	88.5	96.9	106.1
Bulk modulus	170.3	173.1	167	168	166.8	173.6	194.9	193.8	193.6	193.6	157.5	181.8	197.3
Shear modulus	86.06	87.5	–	81.8	–	–	–	–	–	93.9	74.2	71.1	82.3
Young's modulus	222.7	224.7	–	211.4	–	–	–	–	–	242.5	191.8	188.7	216.8
Poisson's ratio	0.289	0.284	–	0.29	–	–	–	–	–	0.291	0.297	0.330	0.329

which represents a good fitting for the stresses in the lattices considered.

Additionally, the forces in a distorted lattice are considered. Several AIMD simulations at different temperatures have been performed for the  $4 \times 4 \times 4$  supercells of the conventional BCC structure of Fe. The temperatures computed are 400, 600, 800, 1000, and 1200 K. Each of these temperatures induces a different distortion of the lattice, and once the structures are relaxed, a snapshot of the atomic positions and magnetic moments at arbitrary times is then used in the MIP to calculate the corresponding forces. The calculated forces by AIMD and the MIP are then compared and can be seen in Fig. 12. In that figure, each color corresponds to a different spatial direction ( $x$ ,  $y$ , and  $z$ ), where Eqs. (8) and (9) are used with  $\xi = x$ ,  $y$ , and  $z$ , respectively, where the horizontal axis corresponds to AIMD calculations, and the vertical axis represents the MIP predictions.

The behavior shown by the MIP predictions is in concordance to the AIMD calculations at each temperature, where the RMSE for each direction ( $RMSE_x$ ,  $RMSE_y$ , and  $RMSE_z$ ) are displayed in Table IV. There is a slight increase of the error when increasing the temperature, suggesting a small deviation of the cell parameter (atomic volume) and magnetic moment at the relaxation of the MIP with respect to AIMD. The errors are nevertheless in reasonable limits. We conclude that the

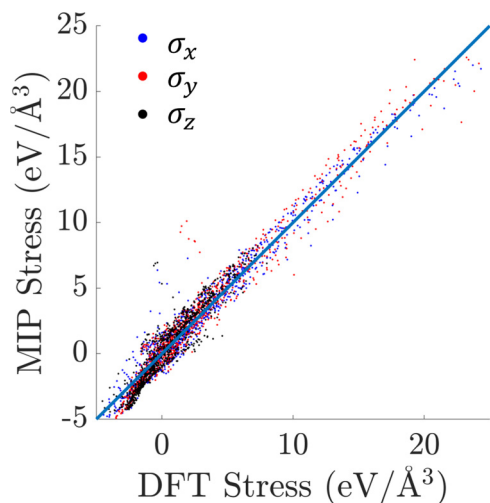


FIG. 11. Comparison of the computed stresses by density functional theory (DFT) and magnetic interatomic potential (MIP).

MIP is accurate enough to represent the behavior of distorted lattices in FM Fe, with atomic positions and magnetic moments deviating from their ideal positions.

### 3. Transformation paths

For this section, several transformation paths are considered. DFT calculations are extracted from Ref. [47], where the spin-polarized DFT calculations were performed using the VASP code, as described elsewhere [71,72,95], with the constant magnetic moment corresponding to the BCC ground state. The transformations considered are the hexagonal, trigonal, tetragonal, and orthorhombic paths, as described in Refs. [96,97], where the parameter  $p$  is continuously varying to drive the transformation, and it can be used to characterize

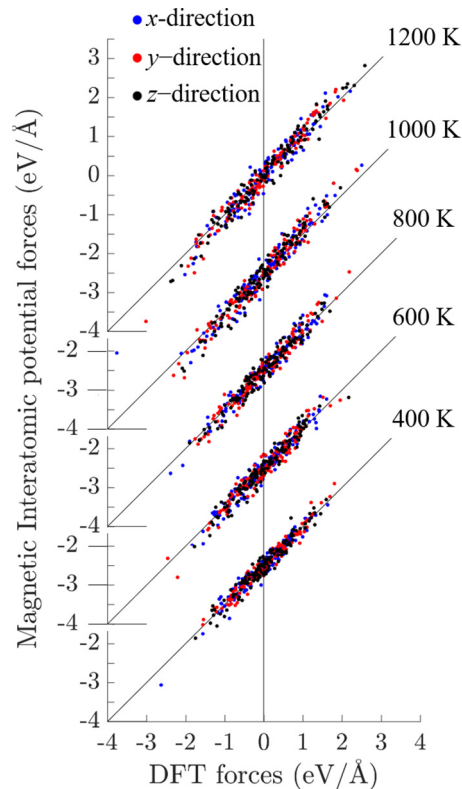


FIG. 12. Comparison of the computed forces by *ab initio* molecular dynamics (AIMD) and the magnetic interatomic potential (MIP) at different temperatures.

TABLE IV. Calculated RMSE of the force predictions of MIP compared with AIMD for each spatial direction at different temperatures.

Temperature (K)	RMSE <sub>x</sub> (eV/Å)	RMSE <sub>y</sub> (eV/Å)	RMSE <sub>z</sub> (eV/Å)
400 K	0.1455	0.1305	0.1522
600 K	0.1750	0.1764	0.1654
800 K	0.1722	0.1717	0.1741
1000 K	0.2188	0.2121	0.2330
1200 K	0.2418	0.2191	0.2081

it. The value  $p = 1$  corresponds in all cases to the BCC structure. The trigonal transformation produces a simple cubic (SC) structure at  $p = 2$  and FCC at  $p = 4$ . The hexagonal path displays a HCP structure at  $p = \sqrt{2}$ . In the tetragonal transformation, the FCC lattice is also reached at  $p = \sqrt{2}$  and body-centered tetragonal (BCT) around  $p = 1.7$ , where in the orthorhombic, the transformation starts and finishes in BCC, passing through the BCT structure around  $p = 1.4$ .

The results are shown in Fig. 13, where the MIP predictions are depicted as blue solid lines and compared with the DFT (black dots) and BOP calculations (red solid lines), both extracted from Ref. [47]. The figure displays the different obtained structures obtained as the transformation occurs.

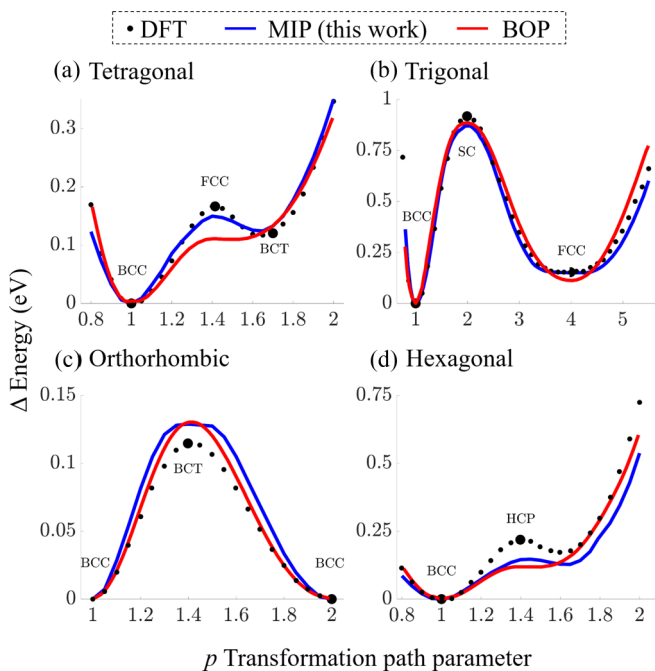


FIG. 13. Transformation paths computed with magnetic interatomic potential (MIP) and compared with density functional theory (DFT) and bond order potential (BOP) from Ref. [47]. Black dots correspond to DFT calculation, red solid line represents the BOP predictions, while the blue solid line corresponds to the MIP calculated transformation paths. Larger black dots represent the different structures obtained with the transformations.  $\Delta$  Energy refers to the difference in energy with respect to the energy of the ground state of body-centered cubic (BCC) iron.

The behavior of the predictions is correct in general, although there is a clear underestimation of the energy in the hexagonal transformation paths with respect to DFT predictions in the HCP crystal lattice. This result is shared with BOP [47], where a similar underestimation in the HCP is also displayed. Nevertheless, BOP also shows a sensible underestimation of the FCC energy (with magnetic contribution), as seen in tetragonal and trigonal transformation paths, whereas the MIP represents these transformations more faithfully. This is a consequence of the correct prediction of the MIP (as shown in previous sections) in the large database employed, which contains the FCC crystal lattice at different magnetic moments.

#### 4. A15 and C15 crystal structures

The analysis of C15 Laves crystal structure is especially relevant for iron since clusters with C15 crystal lattice form under irradiation or after migration of SIAs [98,99]. The development of potentials to predict their behavior is especially important since the experimental observation of small clusters has not been yet achieved, and simulation seems to be the only option available [98,99].

On the other hand, A15 is a metastable structure in BCC metals [100] due to its small energy difference with the ground state. It is considered the simplest complex structure [101]. Therefore, its analysis is the first inevitable step for more complex structures. In other transition metals, this structure is related to superconductivity, its study being full of relevance [102].

In both A15 and C15 structures, there are two positions of atoms that are nonequivalent from the point of view of crystallographic space group symmetry. Nevertheless, the lattice symmetry concept concerning atomic distances must be modified when magnetic moments, which are oriented to a specific coordinate, are introduced. That implies that, in the eight lattice coordinates of the A15 structure (6 + 2 nonequivalent symmetry coordinates), five different nonequivalent symmetry magnetic coordinates (2 + 2 + 2 + 1 + 1) can be obtained. This can be visualized in Fig. 14(b), where the atoms in red, green, and dark blue belong to the same coordinate symmetry but not to the same magnetic coordinate symmetry, as they lie in  $x$ - $y$ ,  $x$ - $z$ , and  $y$ - $z$  planes. This also applies to the C15 symmetry, where the 4 + 2 nonequivalent atomic coordinates have 1 + 1 + 1 + 1 + 2 nonequivalent magnetic coordinate symmetry, as observed in Fig. 14(b).

A set of DFT simulations has been carried out at different atomic volumes, ranging from 8 to 15 Å<sup>3</sup>/atom in steps of 0.2 Å<sup>3</sup>/atom. This refers to lattice parameters between 4.00 and 4.93 Å for the A15 structure and between 5.77 and 7.11 Å for the C15 structure. This range broadly covers the BCC ground state volume and allows analyzing the response of the potential to these structures. For each volume considered, the atoms keep in their ideal positions, while the magnetic moments are relaxed until the ground state is reached. For the case of DFT calculations, the magnitudes of magnetic moments of all atoms are optimized using self-consistent DFT calculations.

The corresponding simulation using the MIP can be seen along with the DFT calculations in Fig. 14(a). The fitting

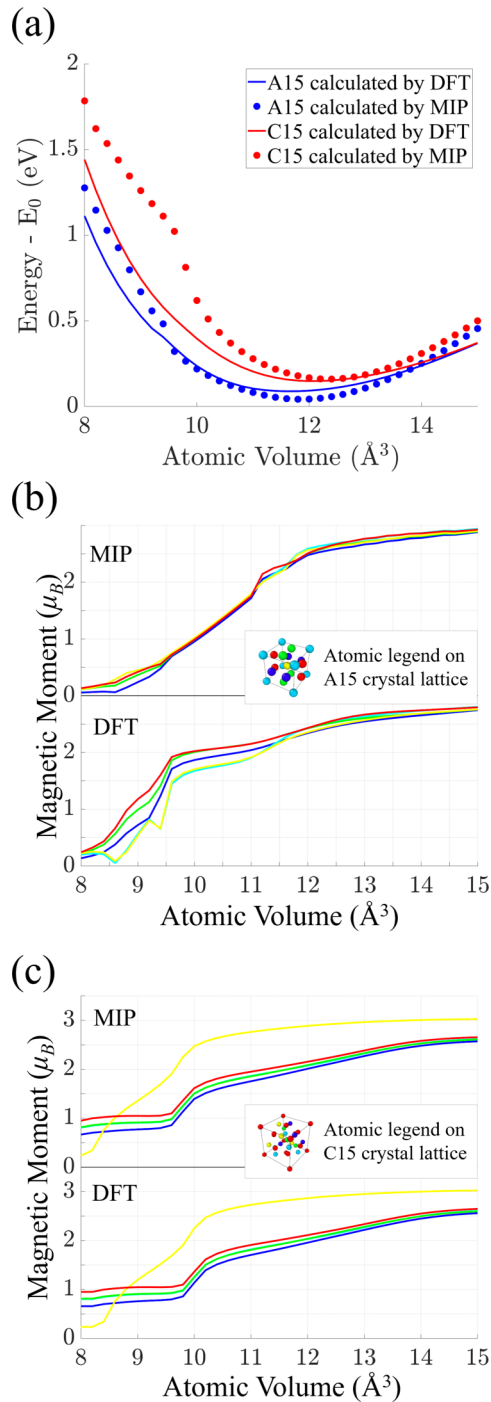


FIG. 14. (a) Density functional theory (DFT) and magnetic interatomic potential (MIP) calculated energy of A15 and C15 with various fixed volumes and relaxed magnetic moments. (b) Variation of the magnetic moment of each atom in the A15 crystal lattice as a function of the volume (the colors correspond to the colors of the atoms in the displayed crystal lattice). (c) Variation of the magnetic moment of each atom in the C15 crystal lattice as a function of the volume (the colors correspond to the colors of the atoms in the displayed crystal lattice).

is reasonably accurate, especially in the vicinities of both the A15 and C15 ground states. The minimum of energy calculated for the C15 lies between 12 and  $12.2 \text{\AA}^3/\text{atom}$  (no

interpolation has been made), and it has an energy difference with the Fe ground state  $\Delta E = E - E_0 \approx 0.148 \text{ eV/atom}$ , where  $E$  represents the corresponding energy and  $E_0$  the BCC ground state energy, like the one obtained in Ref. [99], which predicts  $0.15 \text{ eV/atom}$ . Calculation by the MIP provides a minimum energy between  $12.2$  and  $12.4 \text{\AA}^3/\text{atom}$  with  $\Delta E \approx 0.159 \text{ eV/atom}$ , providing an error in volume  $< 0.2 \text{\AA}^3/\text{atom}$  and an error in energy  $\sim 0.01 \text{ eV}$ . Also in Ref. [99], the corresponding prediction using ABOP is of  $0.14 \text{ eV/atom}$ , showing a similar error to the DFT. On the other hand, the DFT calculations of the A15 crystal lattice predict a minimum energy between  $11.6$  and  $11.8 \text{\AA}^3/\text{atom}$  and  $\Delta E \approx 0.088 \text{ eV}$ , while the MIP provides a minimum  $\sim 11.8\text{--}12 \text{\AA}^3/\text{atom}$  and  $\Delta E \approx 0.042 \text{ eV}$ , which corresponds to an error in volume  $< 0.2 \text{\AA}^3/\text{atom}$  and an error in energy  $\sim 0.04 \text{ eV}$ .

There is a clear step in the curve shape in all DFT and MIP calculations between  $9$  and  $10 \text{\AA}^3/\text{atom}$ . The magnitude of the step is definitely larger in MIP calculations and corresponds to the transition of the magnitudes of the magnetic moment in the simulations by means of the volume. This variation can be observed in Fig. 14(b) for the A15 case and in Fig. 14(c) for the C15 case. The colors correspond to different atoms in the structure, where a label with these colors is depicted in the form of a crystal lattice for each case. In this step and from these atomic volumes toward smaller values, the prediction decreases in accuracy. It is worth noting nevertheless that the range of volumes used in the potential fitting lies between  $9.25$  and  $12.75 \text{\AA}^3/\text{atom}$ , which is close to the limit at which the prediction is less accurate.

In both the C15 and A15 simulations, the magnitude of the magnetic moment increases with the volume. This is, in general, a common result for iron, and it is a consequence of the  $V_g^i(\rho, \mathbf{M})$  function depicted in Fig. 4(b). As a reminder,  $V_g^i(\rho, \mathbf{M})$  represents the volume at which the energy is minimum, given a crystal lattice. Therefore, the simultaneous increase of the volume and the magnetic moment occurs naturally.

## 5. Vacancy

In this section, we will consider a vacancy simulation with relaxed atomic coordinates, volume, and magnetic moments. The simulation is performed with both DFT and MIP methods for comparison purposes, using the same configuration, a structure of  $4 \times 4 \times 4$  supercells of the conventional BCC structure of Fe with one vacancy, containing 127 atomic sites. As in the case of calculations for the A15 and C15 structures, for the case of DFT calculations, the magnitudes of magnetic moments of all atoms are optimized using self-consistent DFT calculations. For the case of the MIP, molecular static simulations using the proposed equations of motion for the MIP in Eq. (8) allow obtaining the corresponding minimum configuration energy.

After relaxation, the obtained energy of formation for 127 atoms using DFT is  $2.14 \text{ eV}$ , which is in accordance with the formation energy of vacancy reported [22,103,104] using also DFT. The corresponding value for the MIP is  $1.65 \text{ eV}$ , being moderately lower. This may be because the second nearest neighbors of the vacancy are the only atoms displaying

TABLE V. Comparison of the energy of formation of vacancy  $E_v^f$  with MIP and DFT (this paper) and other obtained  $E_v^f$  in the literature by different approaches.

Method	Ref.	$E_v^f$ (eV)
MIP	This paper	1.65
DFT	This paper	2.14
	[22]	1.95, 1.93, 2.07
	[103]	2.12, 1.93
	[104]	2.18, 2.26
Empirical potential	[17,105]	1.37/1.70
	[21]	1.63/1.95
	[106]	1.57/1.63
LML	[91]	2.14
QNML	[91]	2.18
Experiment	[107]	1.6
	[108]	1.8

a significant increase of energy with respect to the BCC equilibrium, about  $\Delta E \approx 0.1$  eV per atom, as compared with the equilibrium, while the following neighbor atoms in the distance to the vacancy have a  $\Delta E$  in the range of 0.01 eV. This increase of energy is slightly underestimated as compared with the DFT calculations. A summary of both DFT and MIP results are compared in Table V with others reported in the literature using atomistic simulations and obtained by experiment.

The results of the crystal lattices obtained by DFT and the MIP in this paper are displayed in Fig. 15, showing a similar behavior. The first nearest neighbors of the vacancy in the DFT are displaced toward the vacancy 0.085 Å along with an increase of magnetic moment of  $\sim 0.2 \mu_B$ , while in the case of the MIP, the displacement is 0.06 Å along with an increase of  $0.1 \mu_B$ . These correspond to the atoms displayed in red. On the other side, the second nearest neighbors of the vacancy move away from the vacancy 0.03 Å and suffer a decrease of the magnetic moment of  $\sim 0.2 \mu_B$ , while in the simulation with the MIP, the atom is similarly displaced away from the vacancy 0.04 Å along with a decrease of  $0.1 \mu_B$ , with respect to the magnetic moment at the ground state. The third nearest neighbors have negligible variations with respect to both the ideal atomic coordinates and ground state magnetic moments.

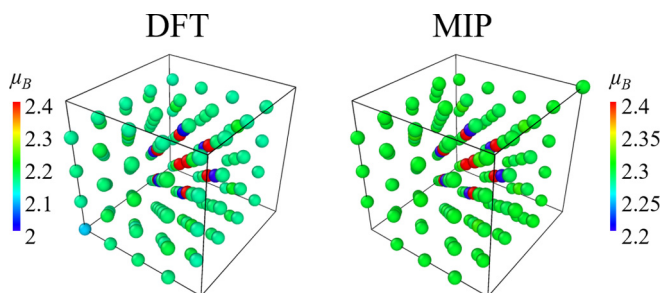


FIG. 15. Atomic coordinates of relaxed vacancy simulation with density functional theory (DFT) and magnetic interatomic potential (MIP). The colors of the atoms correspond to the magnetic moment as displayed by the legends.

With the MIP formulation, the variation on the magnetic moment magnitude observed in the first and second nearest neighbors, compared with the rest of the atoms, can be explained. Firstly, we should focus our attention to the functions  $\omega_0(\rho_{ij})$  and  $\omega_M(\rho_{ij})$  displayed in Fig. 8(a). As a reminder, the values of  $\rho_{ij}$  for the first and second nearest atoms in a BCC structure are 1.299 and 2, respectively. In consequence, an atom in the position of the first nearest neighbor of the vacancy is missing a positive term at evaluating  $\omega_0(\rho_{ij})$  and  $\omega_M(\rho_{ij})$  (at a distance  $\rho_{ij} = 1.299$ ) in the whole sum of atoms. Therefore, the corresponding values of  $E_g^i(\rho, M)$ ,  $V_g^i(\rho, M)$ , and  $V_g^i(\rho, M)$  are smaller than in the perfect BCC crystal lattice, in the range of 0.005 eV,  $0.1 \text{ \AA}^3$ , and  $0.01 \text{ \AA}^3$ , respectively. Inversely, the value of the  $E_g^i(\rho, M)$ ,  $V_g^i(\rho, M)$ , and  $V_g^i(\rho, M)$  parameters for the second nearest neighbors of the vacancy are larger than in the perfect BCC crystal lattice, in the range of 0.02 eV,  $0.1 \text{ \AA}^3$ , and  $0.01 \text{ \AA}^3$ , respectively, since, in this case, a term (at a distance  $\rho_{ij} = 2$ ) is missing when evaluating  $\omega_0(\rho_{ij})$  and  $\omega_M(\rho_{ij})$ . The evaluation of these parameters and the corresponding values of  $\frac{dE_g^i}{dM_i}$ ,  $\frac{dV_g^i}{dM_i}$ , and  $\frac{dK_g^i}{dM_i}$  [see Eq.(9)] for a constant magnetic moment across all atoms show positive magnetic forces for the first nearest neighbor of the vacancy and negative magnetic forces for the second nearest neighbor of the vacancy, explaining the variation of the magnetic moments observed.

## 6. Dumbbell configurations

An analysis of the performance of the MIP with respect to  $\langle 110 \rangle$ ,  $\langle 111 \rangle$ , and  $\langle 100 \rangle$  dumbbell configurations has been done and compared with the DFT calculations. The self-consistent DFT calculations were performed with a relaxation of atomic positions for eight different volumes with lattice parameters ranging from 2.6448 to 2.9434 Å. Using a  $4 \times 4 \times 4$  BCC simulation box with 129 atoms, different cell parameters have been considered to cover the dumbbell ground state. For each volume, both the atomic coordinates and magnetic moments are relaxed.

The results are displayed in Fig. 16, where the  $\langle 110 \rangle$  configuration is shown in black color, the  $\langle 111 \rangle$  configuration is plotted in blue color, while the  $\langle 100 \rangle$  is finally depicted in red color. The DFT calculations correspond to dashed lines with solid squares, and the MIP predictions are shown with solid lines and circles.

In both simulations, the  $\langle 110 \rangle$  dumbbell configuration is the most stable of all, followed by the  $\langle 111 \rangle$  configuration. The  $\langle 100 \rangle$  case is, therefore, the least energetically favorable. The equilibrium cell parameter of the MIP is slightly larger than in DFT calculations, in correspondence to the larger unit cell parameter of BCC iron calculated by the MIP.

The formation energies and equilibrium cell parameters for both types of calculations can be seen in Table VI along with others reported in the literature. The DFT formation energies in this paper are like the corresponding ones computed also by DFT in Ref, [22], with a slightly larger difference in the  $\langle 100 \rangle$  dumbbell configuration. Minor differences are found with MEAM and empirical potential predictions, although it is worth noting that some works predict that the  $\langle 111 \rangle$  dumbbell has lower formation energy than the  $\langle 110 \rangle$  dumbbell, in

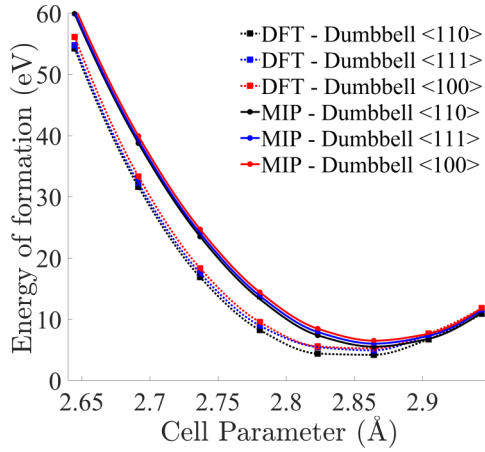


FIG. 16. Formation energy of the dumbbell  $\langle 110 \rangle$ ,  $\langle 111 \rangle$ , and  $\langle 100 \rangle$  configurations in a  $4 \times 4 \times 4$  body-centered cubic (BCC) simulation box as a function of the unit cell parameter. For each cell parameter considered, both the atomic coordinates and magnetic moments are relaxed.

contradiction to the DFT calculations reported here and others (both DFT and empirical potentials). With respect to the MIP predictions, the formation energy is in the range of 1–1.5 eV as compared with the DFT ones, and the equilibrium sequence is correctly computed. Additionally, the MIP prediction of the ground state (GS) unit cell parameter is of the order of 0.025 Å larger than the corresponding DFT calculations.

A visualization of the relaxed lattice is also helpful in validating the MIP performance at predicting SIAs. In the following figures, a comparison of the relaxed structures at their respective GS is shown. Figure 17(a) shows the comparison of the  $\langle 110 \rangle$  dumbbell configuration, Fig. 17(b) corresponds to the  $\langle 111 \rangle$  case, while Fig. 17(c) represents the  $\langle 100 \rangle$  case. Each figure shows the different perspectives of the simulation box, avoiding the plotting of the equivalent perspectives [for instance, perspectives  $(x, z)$  and  $(y, z)$  are equivalent in the

TABLE VI. Formation energies, corresponding relaxation volume of  $\langle 110 \rangle$ ,  $\langle 111 \rangle$ , and  $\langle 100 \rangle$  dumbbell configurations using DFT and MIP in this paper. The relaxation volume stands for the difference in a  $4 \times 4 \times 4$  BCC simulation box. The formation energies are compared with others reported in the literature.

	Method and reference	$\langle 110 \rangle$	$\langle 111 \rangle$	$\langle 100 \rangle$
Relaxation volume ( $\text{Å}^3$ )	MIP (this paper)	12.8	15.9	22.2
	DFT (this paper)	19.3	18.9	21.3
Formation energies (eV)	MIP (this paper)	5.5	6.0	6.5
	DFT (this paper)	3.9	4.6	5.5
	DFT [22]	3.64	4.34	4.64
	DFT [47]	3.93	4.61	5.05
	BOP [47]	3.87	4.22	4.44
	MEAM [109]	4.2	4.3	5.5
	Empirical potential [101]	3.93	3.98	–
	Empirical potential [110]	4.06	3.92	–
	Empirical potential [111]	4.85	–	–
	Empirical potential [17]	4.87	5	6.1
	Empirical potential [106]	4.15	4.34	–

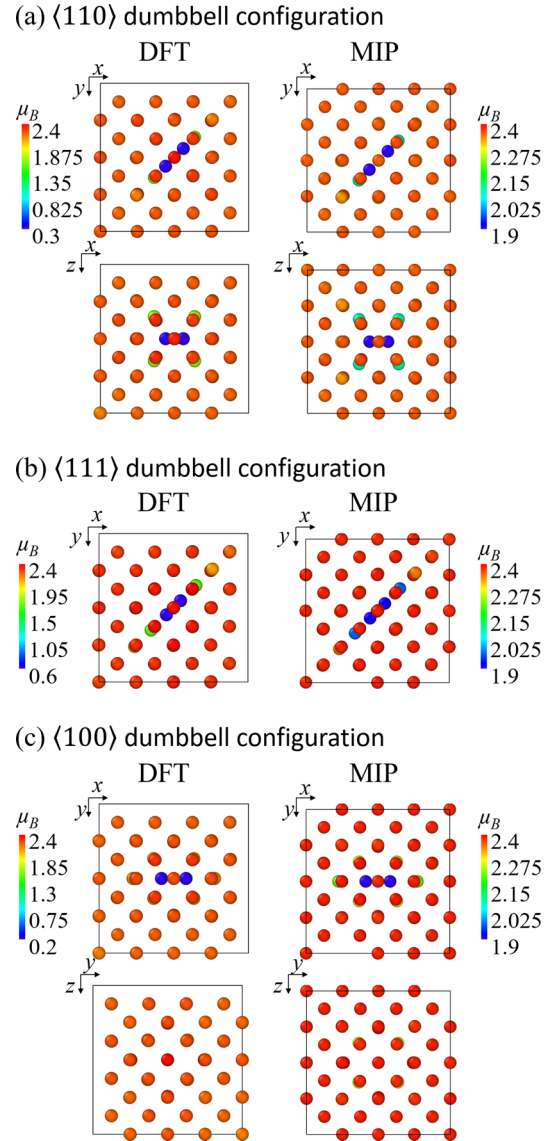


FIG. 17. (a) Atomic configuration of  $\langle 110 \rangle$  dumbbell configuration at the volume corresponding to the ground state. Perspectives  $(x, z)$  and  $(y, z)$  are equivalent. (b) Atomic configuration of  $\langle 111 \rangle$  dumbbell configuration at the volume corresponding to the ground state. Perspectives  $(x, y)$ ,  $(x, z)$ , and  $(y, z)$  are equivalent. (c) Atomic configuration of  $\langle 100 \rangle$  dumbbell configuration at the volume corresponding to the ground state. Perspectives  $(x, y)$  and  $(x, z)$  are equivalent.

$\langle 110 \rangle$  configuration]. The colors of each atom correspond to the magnitude of its magnetic moment.

The results show that the atoms accommodate in the available space, displacing neighboring atoms outside the interstitial positions. As a rule, the MIP and DFT simulations display minor differences with respect to the relaxed atomic coordinates. Concerning the magnetic moments, the overall behavior is the same, showing a decrease in the values of the SIAs. The lower the atomic volume, the lower the magnitude of the magnetic moment. The SIAs display therefore the lowest magnetic moments, followed by the displaced surrounding atoms. The effect on the third and forthcoming nearest



neighbors is minimum. The main difference between the DFT and MIP calculations is the magnitude of that variation of the magnetic moment. In all cases, the reduction of the magnetic moment in DFT is much more pronounced, reaching values  $\sim 0.2\text{--}0.6 \mu_B$ , while in the MIP case, the minimum values lie  $\sim 1.9 \mu_B$ . The reason for that difference could be the fact that the original fitting data do not have atoms so close nor lattices with strong differences in magnetic moments along with their atoms. This does not demerit the prediction made by the MIP, which is considered correct in general, although there is room for improvement.

### 7. $\gamma$ surfaces

Generalized stacking faults, or  $\gamma$  surfaces, in BCC materials are closely related to the dislocation core fields [112]. The  $\{110\}$  and  $\{211\}$   $\gamma$  surfaces represent initial simple calculations to obtain information about the dislocation predicted behavior [38].

For this section, no particular DFT calculation has been performed in this paper since data are available from previous publications [38,47,113]. The MIP simulations have been performed using a bicrystal geometry, dividing the crystal along the  $z$  direction. The upper crystal is displaced along the  $x$  and  $y$  directions, and only atomic coordinate relaxation in the  $z$  direction is allowed as well as the magnitudes of the magnetic moment per atom. The  $\{110\}$   $\gamma$  surface is created when displaced toward the  $\langle 1\bar{1}0 \rangle$  and  $\langle 001 \rangle$  directions, and the  $\{211\}$   $\gamma$  surface corresponds to translations toward the  $\langle 111 \rangle$  and  $\langle 110 \rangle$  directions. For the  $\{110\}$   $\gamma$ -surface simulations, the  $x \times y \times z$  box size is  $6 \times 4\sqrt{2} \times 36 \sqrt{2}$  in units of the cell parameter ( $\sim 17.15 \times 16.17 \times 145.58 \text{ \AA}^3$ ) corresponding to 3456 atoms in 72 atomic layers in the  $z$  direction, while in the  $\{211\}$   $\gamma$ -surface simulations, the box size is  $4\sqrt{3} \times 4\sqrt{2} \times 18 \sqrt{6}$  in units of the cell parameter ( $\sim 19.81 \times 16.17 \times 126.08 \text{ \AA}^3$ ), corresponding also to 3456 atoms in 108 atomic layers in the  $z$  direction. In both simulations, a few top and bottom atomic layers are frozen. The simulations are large enough to avoid size effects since a few dozens of atomic layers are allowed to relax. Nevertheless, the size of the simulation box is substantially larger than in DFT simulations, and hence, there is probably more room for relaxation, and lower energies may be expected.

Before the analysis of both the  $\{110\}$  and  $\{112\}$   $\gamma$ -surfaces, the  $\frac{1}{2}\langle 111 \rangle$  screw dislocation is under consideration due to its importance in controlling the BCC plastic behavior. The energy variation along the  $[110]$  direction can be extracted from the  $\{110\}$   $\gamma$  surface easily, and the results can be seen in Fig. 18 compared with DFT [113] and BOP [47]. The results show a similar behavior of the MIP compared with both DFT and BOP methodologies, although an underestimation of the energy  $\sim 25 \text{ meV/\AA}^2$  with respect to DFT prediction is observed. This difference can be attributed to the size of the simulation box, although an inherent error from the MIP cannot be discarded.

The results of the  $\{110\}$  and  $\{112\}$   $\gamma$  surfaces are shown in Fig. 19. The MIP predictions correctly display the dependence of the energy in both the  $\{110\}$  and  $\{211\}$   $\gamma$  surfaces, both in shape and in magnitude in comparison with the DFT results shown [38]. In the  $\{110\}$   $\gamma$  surface, the maximum value

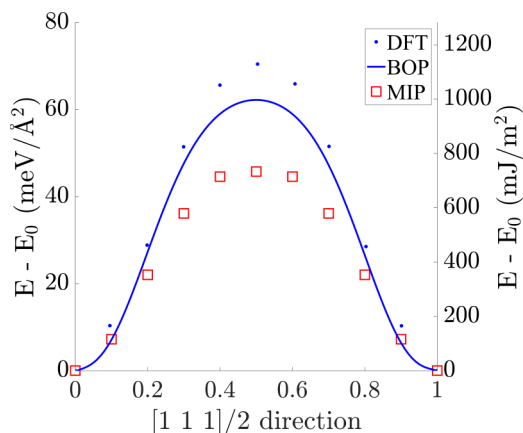


FIG. 18.  $[110]$  cross-section of the relaxed  $\{110\}$   $\gamma$  surface using density functional theory (DFT), bond order potential (BOP), and magnetic interatomic potential (MIP) relaxed calculations.

occurs at  $0.5b$  of both the  $\langle 1\bar{1}0 \rangle$  and  $\langle 001 \rangle$  vectors, where  $b$  represents the Burgers vector, with a value  $\sim 90 \text{ meV/\AA}^2$ . For the case of DFT calculations, this maximum is slightly  $>100 \text{ meV/\AA}^2$ , suggesting a small underestimation of the predicted energy. A similar underestimation seems to occur in the  $\{211\}$   $\gamma$  surface simulations, where the maximum occurs at  $b/2$  of  $\langle 110 \rangle$  and  $b/3$  of  $\langle 111 \rangle$ .

In the MIP simulations obtained, there is a clear correlation between the volume of the atomic layers and the corresponding magnetic moment. A visualization of this effect can be seen in Fig. 20 for both  $\{110\}$  and  $\{211\}$   $\gamma$  surfaces. The horizontal axis corresponds to the distance along the  $z$  direction between stacking planes (only the nearest to the

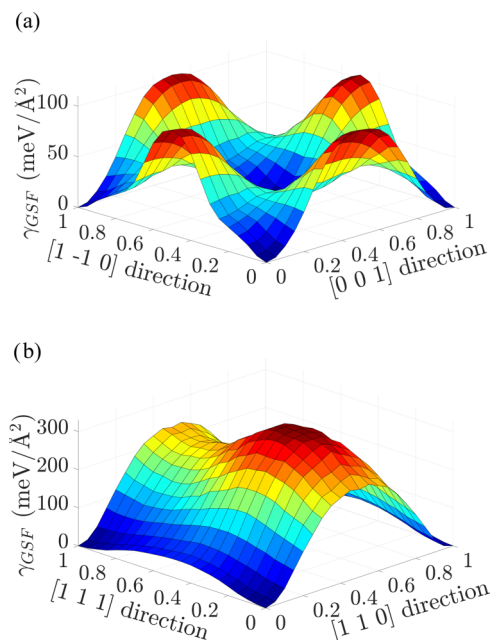


FIG. 19. (a) Relaxed  $\{110\}$   $\gamma$  surface using magnetic interatomic potential (MIP). (b) Relaxed  $\{112\}$   $\gamma$  surface using MIP. The  $x$  and  $y$  axes are given in reduced units. The results can be compared with figs. 4(a) and 4(b) of Ref. [38].

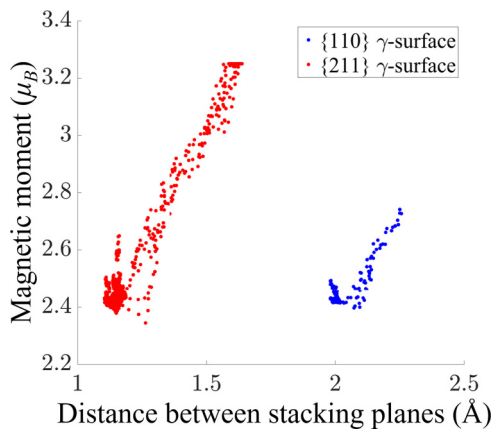


FIG. 20. Relation between the distance between faulted stacking planes in the  $\{110\}$  and  $\{211\}$   $\gamma$ -surface magnetic interatomic potential (MIP) simulations and the corresponding magnetic moment variation per layer.

fault). The vertical axis represents the associated magnetic moment of the atomic layers. Two main things must be noted before interpreting this figure: firstly, the staking distance in the  $\{110\}$   $\gamma$  surface (blue dots) is larger than in the  $\{211\}$   $\gamma$  surface (red dots); and secondly, although the distance along the  $z$  direction between stacking planes is not the atomic volume, they are indeed correlated. The larger the stacking distance, the larger the atomic volume. Considering this, the main behavior is a linear increase of the magnetic moment along with the volume. This correlates well with the  $V_g^i(\rho, M)$  behavior, as plotted in Fig. 4(b). The behavior of the BCC lattice, as indicated in the figure,  $V_g^i(\rho, M)$  increases linearly as a function of the volume, especially around the magnetic moment between 1 and  $3.25 \mu_B$ . This upper limit is the maximum value considered in the original data, and the MD simulations do not allow larger values. This maximum value is clearly seen in the  $\{211\}$   $\gamma$ -surface red dots in Fig. 20 and suggests that larger values of the magnetic moment must be included if larger volumes are considered. This is reflected in Fig. 19(d), where the  $\{211\}$   $\gamma$  surface calculated by the MIP displays a rough surface in the vicinities of the maximum values (corresponding to  $0.5b$  of  $\{110\}$  and  $b/3$  of  $\{111\}$ ), as a consequence of the larger volumes and magnetic moments needed to converge property.

Another consequence of this analysis is the larger energy obtained in the  $\{211\}$   $\gamma$  surface than in the  $\{110\}$   $\gamma$  surface. The wider variation in volume must be accompanied by a wider variation in energy. This is because  $E_g^i(\rho, \mathbf{M})$  and  $V_g^i(\rho, \mathbf{M})$  are related, as in Figs. 4(a) and 4(b). Therefore, those BCC layers that need more space to accommodate increase their magnetic moment, corresponding to an increase of the contribution to the energy of those layers.

It is important to note that this analysis is possible thanks to the behavior observed when studying the behavior of the parameters that define the UES. This analysis is indeed difficult to perform in previously reported potentials with the magnetic contribution. In the current proposed potential, the overall behavior of a lattice can be anticipated at a certain level thanks to the interrelationship of the UES parameters.

## VI. CONCLUSIONS

In this paper, we have generalized the UES defined by Vinet *et al.* [56] and Rose *et al.* [55] to include the effect of magnetism. For a certain lattice and fixed magnetic configuration, the behavior of the energy by means of volume variations is captured with good accuracy by this GUES. This result extends the predictive capabilities of the original UES and allows the exploration of formulations to describe the behavior of the GUES parameters, namely,  $E_g^i(\rho, \mathbf{M})$ ,  $V_g^i(\rho, \mathbf{M})$ , and  $K_g^i(\rho, \mathbf{M})$ , related to the energy and volume at the local ground state and dependent on the interatomic distances and magnetic configuration.

When examining their behavior for the NM case, we have found a surprising result since they behave identically once they are properly scaled to the quantities they represent. For an increase of  $E_g^i(\rho, M)$ , which represents the ground state energy at each configuration, an increase of  $V_g^i(\rho, M)$  follows, its respective volume at this ground state, and a similar increase of  $K_g^i(\rho, M)$ , the scale volume. This allowed defining a unique function  $\omega_0(\rho_{ij})$  to describe them all with respect to the interatomic atomic distances.

The behavior of the  $E_g^i(\rho, M)$ ,  $V_g^i(\rho, M)$ , and  $V_g^i(\rho, M)$  functions with respect to the magnetic moment has shown that an additional and common function,  $\omega_M^{FM}(\rho_{ij})$  and  $\omega_M^{AFM}(\rho_{ij})$  for the FM and AFM, respectively, dependent also on the interatomic distances is needed to include the magnetic influence on the potential. The magnetic influence on the GUES is introduced by two magnetic functions per parameter. When evaluating the contribution of atom  $i$  to the energy, the first ones denoted  $\Phi_E(M_i)$ ,  $\Phi_V(M_i)$ , and  $\Phi_K(M_i)$  depend only on the magnetic moment  $M_i$  of this atom. Being dependent on the magnetic moment of the atom isolated, their contribution to the energy is logically independent of the interatomic distances to other atoms in the lattice. On the other hand, the second set of functions depends on the interaction of the magnetic moment of atom  $i$  and the magnetic moment of its neighboring atoms  $\Psi_E(M_i, M_j)$ ,  $\Psi_V(M_i, M_j)$ , and  $\Psi_K(M_i, M_j)$ . These in turn are scaled by a unique distance-dependent function  $\omega_M(\rho_{ij})$  [correspondingly  $\omega_M^{FM}(\rho_{ij})$  or  $\omega_M^{AFM}(\rho_{ij})$ ] to account for the decreasing influence of the atoms when increasing the interatomic distance. Both  $\Phi$  and  $\Psi$  magnetically dependent functions are described by even polynomials for both the FM and AFM cases.

These magnetic functions have been fitted to describe the energy calculations using DFT data for the case of FM and AFM iron, and the formulation has been proved to provide good predictability of the energy on all DFT data calculated, incorporating both magnetic configurations.

Although the formulation in its current state demands different distance and magnetically dependent functions for different magnetic configurations, the novel approach paves the way to developing interatomic potentials to predict DFT calculations with magnetic contribution and is consistent with previous approaches for describing magnetism, as the Stoner model of band magnetism and the approximation proposed by the Ginzburg-Landau model. Also, to be consistent with interlattice-site Heisenberg magnetic interaction parameters of the Heisenberg-Landau Hamiltonian, the dependence of the  $\Psi_E(M_i, M_j)$ ,  $\Psi_V(M_i, M_j)$ , and  $\Psi_K(M_i, M_j)$  functions are

defined so that the magnetic moments of different atoms  $M_i$  and  $M_j$  are introduced by multiplication of their magnitudes  $M_i M_j$ .

A FM MIP has been finally developed after the definition of the explicit expressions of  $\omega_0(\rho_{ij})$  and  $\omega_M(\rho_{ij})$  distance-dependent functions. This demonstrates that  $\omega_0(\rho_{ij})$  and  $\omega_M(\rho_{ij})$  functions exist, and they can be used for describing the energy of the system along with the corresponding magnetically dependent functions. The prediction of the LS and HS states has also been studied and provides similar results as the ones reflected by DFT calculations, with minor differences.

The dependence of the  $\Psi_E(M_i, M_j)$ ,  $\Psi_V(M_i, M_j)$ , and  $\Psi_K(M_i, M_j)$  functions as a function of the multiplication of the magnetic moments has allowed assessing the predictability of the potential outside the database employed for its development in structures with a larger degree of complexity. The potential has been applied to perform simulations in different lattices, prediction of elastic constants, vacancies, interstitials, and transformation paths as well as  $\gamma$  surfaces with good accuracy and exceptional predictability, not only in the energy but in the behavior of the atomic coordinates and magnetic moment at relaxing. The MIP cannot replace the DFT method, but it can incorporate magnetism in a novel approach, providing a tool for accelerating large-scale atomistic simulations with reasonable precision.

The use of the GUES as a source for the development of potentials has shown clear advantages since it generalizes and incorporates the use of magnetism into the calculation of the energy of a system. There are nevertheless many aspects that claim attention, and further investigation is needed. To be consistent with other forms of magnetism, the formulations must be adapted or completed to include, among others, AFM configurations so that an interatomic potential can be developed with this magnetic configuration. The implementation into the MD approach induces a revision of the way in which the atomic coordinates, magnetic moment, and volume vary with the time since they work at different levels. The variation of the magnetic moment may occur much faster than the displacement of the atoms, but they are connected in this formulation, and one cannot be conceived without the other.

Another aspect that requires attention is the possible existence of unique distance-dependent  $\omega_0$  and  $\omega_M$  functions as well as  $\Phi$  and  $\Psi$  magnetically dependent functions for other magnetic elements and lattices. An initial analysis in Cr, Ni, Co, and Mn with FM and AFM configurations showed that the GUES is also applicable to other elements, which may open the door to complex systems such as steels and HEAs containing magnetic elements. The physical understanding of these functions passes through a deep analysis of the behavior of the atoms from the electronic point of view. This in turn could pave the way to simulating different atomic species in the same lattice, which is the ultimate purpose of an atomistic simulation.

#### ACKNOWLEDGMENTS

I.T.C. is grateful for financial support of the fellowship 2016-T2/IND-1693, from the Programme Atracción de talento investigador (Consejería de Educación, Juventud y Deporte, Comunidad de Madrid) and the project AFORMAR from the Spanish National Programme—call 2019 «Proyectos de I+D+i» (Ministerio de Ciencia e Innovación). The work of J.S.W. and D.S.M. has been carried out within the framework of the EUROfusion Consortium, funded by the European Union via the Euratom Research and Training Programme (Grant Agreement No 101052200—EUROfusion). Views and opinions expressed are, however, those of the author(s) only and do not necessarily reflect those of the European Union or the European Commission. Neither the European Union nor the European Commission can be held responsible for them. D.N.M. work is also supported by the UK Engineering and Physical Sciences Research Council Grant No. EP/W006839/1. The work at WUT has been carried out as a part of an international project cofinanced from the funds of the program of the Polish Minister of Science and Higher Education entitled “PMW” in 2019; Agreement No. 5018/H2020-Euratom/2020/2. J.S.W. and D.N.M. acknowledge the support from high-performing computing facility MARCONI (Bologna, Italy) provided by EUROfusion. The simulations were also carried out with the support of the Poznan Supercomputing and Networking Center PCSS under Grant No. 274.

- 
- [1] M. S. Daw and M. I. Baskes, Semiempirical, Quantum Mechanical Calculation of Hydrogen Embrittlement in Metals, *Phys. Rev. Lett.* **50**, 1285 (1983).
  - [2] M. S. Daw and M. I. Baskes, Embedded-atom method: derivation and application to impurities, surfaces, and other defects in metals, *Phys. Rev. B* **29**, 6443 (1984).
  - [3] F. Ercolessi and E. Tosatti, Au (100) Surface Reconstruction, *Phys. Rev. Lett.* **57**, 719 (1986).
  - [4] F. Ercolessi, M. Parrinello, and E. Tosatti, Simulation of gold in the glue model, *Philos. Mag. A* **58**, 213 (1988).
  - [5] F. Ercolessi and J. B. Adams, Interatomic potentials from first-principles calculations: the force-matching method, *EPL* **26**, 583 (1994).
  - [6] R. Zivieri, G. Santoro, and V. Bortolani, Multiphonon effects in the one-phonon cross section of Al, *Phys. Rev. B* **58**, 5429 (1998).
  - [7] R. Zivieri, G. Santoro, and V. Bortolani, Anharmonicity on Al(100) and Al(111) surfaces, *Phys. Rev. B* **59**, 15959 (1999).
  - [8] R. Zivieri, G. Santoro, and V. Bortolani, Premelting of the Al(110) surface from a local perspective, *Phys. Rev. B* **62**, 9985 (2000).
  - [9] M. W. Finnis and J. E. Sinclair, A simple empirical  $N$ -body potential for transition metals, *Philos. Mag. A* **50**, 45 (1984).
  - [10] X. D. Dai, Y. Kong, J. H. Li, and B. X. Liu, Extended Finnis-Sinclair potential for bcc and fcc metals and alloys, *J. Phys. Condens. Matter* **18**, 4527 (2006).

- [11] L. Malerba, M. C. Marinica, N. Anento, C. Björkas, H. Nguyen, C. Domain, F. Djurabekova, P. Olsson, K. Nordlund, A. Serra, D. Terentyev, F. Willaime, and C. S. Becquart, Comparison of empirical interatomic potentials for iron applied to radiation damage studies, *J. Nucl. Mater.* **406**, 19 (2010).
- [12] M. I. Mendeleev, M. J. Kramer, C. A. Becker, and M. Asta, Analysis of semi-empirical interatomic potentials appropriate for simulation of crystalline and liquid Al and Cu, *Philos. Mag.* **88**, 1723 (2008).
- [13] C. P. Chui, W. Liu, Y. Xu, and Y. Zhou, Molecular dynamics simulation of iron—a review, *Spin* **5**, 1540007 (2015).
- [14] X. Zhou, M. E. Foster, J. A. Ronevich, and C. W. San Marchi, Review and construction of interatomic potentials for molecular dynamics studies of hydrogen embrittlement in Fe-C based steels, *J. Comput. Chem.* **41**, 1299 (2020).
- [15] M. I. Baskes, *Modified Embedded Atom Method Calculations of Interfaces* (Sandia National Lab, Livermore, 1996).
- [16] B. Jelinek, S. Groh, M. F. Horstemeyer, J. Houze, S. G. Kim, G. J. Wagner, A. Moitra, and M. I. Baskes, Modified embedded atom method potential for Al, Si, Mg, Cu, and Fe alloys, *Phys. Rev. B* **85**, 245102 (2012).
- [17] G. J. Ackland, D. J. Bacon, A. F. Calder, and T. Harry, Computer simulation of point defect properties in dilute Fe-Cu alloy using a many-body interatomic potential, *Philos. Mag.* **A 75**, 713 (1997).
- [18] M. I. Mendeleev, S. Han, D. J. Srolovitz, G. J. Ackland, D. Y. Sun, and M. Asta, Development of new interatomic potentials appropriate for crystalline and liquid iron, *Philos. Mag.* **83**, 3977 (2003).
- [19] C. S. Becquart, J. M. Raulot, G. Bencteux, C. Domain, M. Perez, S. Garruchet, and H. Nguyen, Atomistic modeling of an Fe system with a small concentration of C, *Comput. Mater. Sci.* **40**, 119 (2007).
- [20] H. C. Herper, E. Hoffmann, and P. Entel, *Ab initio* full-potential study of the structural and magnetic phase stability of iron, *Phys. Rev. B* **60**, 3839 (1999).
- [21] C. Domain and C. S. Becquart, *Ab initio* calculations of defects in Fe and dilute Fe-Cu alloys, *Phys. Rev. B* **65**, 024103 (2002).
- [22] C. C. Fu, F. Willaime, and P. Ordejón, Stability and Mobility of Mono- and Di-Interstitials in A-Fe, *Phys. Rev. Lett.* **92**, 175503 (2004).
- [23] D. Nguyen-Manh, V. Vitek, and A. P. Horsfield, Environmental dependence of bonding: a challenge for modelling of intermetallics and fusion materials, *Prog. Mater. Sci.* **52**, 255 (2007).
- [24] D. Nguyen-Manh, M. Y. Lavrentiev, and S. L. Dudarev, Magnetic origin of nano-clustering and point defect interaction in Fe-Cr alloys: an *ab-initio* study, *J. Comput. Mater. Des.* **14**, 159 (2007).
- [25] M. Y. Lavrentiev, D. Nguyen-Manh, and S. L. Dudarev, Magnetic cluster expansion model for bcc-fcc transitions in Fe and Fe-Cr alloys, *Phys. Rev. B* **81**, 184202 (2010).
- [26] D. Nguyen-Manh, M. Y. Lavrentiev, M. Muzyk, and S. L. Dudarev, First-principles models for phase stability and radiation defects in structural materials for future fusion power-plant applications, *J. Mater. Sci.* **47**, 7385 (2012).
- [27] D. Nguyen-Manh, P. W. Ma, M. Y. Lavrentiev, and S. L. Dudarev, Constrained non-collinear magnetism in disordered Fe and Fe-Cr alloys, *Ann. Nucl. Energy* **77**, 246 (2015).
- [28] M. Y. Lavrentiev, J. S. Wróbel, D. Nguyen-Manh, and S. L. Dudarev, Magnetic and thermodynamic properties of face-centered cubic Fe-Ni alloys, *Phys. Chem. Chem. Phys.* **16**, 16049 (2014).
- [29] J. S. Wróbel, D. Nguyen-Manh, M. Y. Lavrentiev, M. Muzyk, and S. L. Dudarev, Phase stability of ternary fcc and bcc Fe-Cr-Ni alloys, *Phys. Rev. B* **91**, 024108 (2015).
- [30] Z. Leong, S. L. Dudarev, R. Goodall, I. Todd, and D. Nguyen-Manh, The effect of electronic structure on the phases present in high entropy alloys, *Sci. Rep.* **7**, 39803 (2017).
- [31] M. Fedorov, J. S. Wróbel, A. Fernández-Caballero, K. J. Kurzydłowski, and D. Nguyen-Manh, Phase stability and magnetic properties in fcc Fe-Cr-Mn-Ni alloys from first-principles modeling, *Phys. Rev. B* **101**, 174416 (2020).
- [32] J. S. Wróbel, M. R. Zemla, D. Nguyen-Manh, P. Olsson, L. Messina, C. Domain, T. Wejrzanowski, and S. L. Dudarev, Elastic dipole tensors and relaxation volumes of point defects in concentrated random magnetic Fe-Cr alloys, *Comp. Mater. Sci.* **194**, 110435 (2021).
- [33] D. Nguyen-Manh, S. L. Dudarev, and A. P. Horsfield, Systematic group-specific trends for point defects in bcc transition metals: an *ab initio* study, *J. Nucl. Mater.* **367–370**, 257 (2007).
- [34] G. Liu, D. Nguyen-Manh, B. G. Liu, and D. G. Pettifor, Magnetic properties of point defects in iron within the tight-binding-bond Stoner model, *Phys. Rev. B* **71**, 174115 (2005).
- [35] D. Nguyen-Manh and S. L. Dudarev, Model many-body Stoner Hamiltonian for binary FeCr alloys, *Phys. Rev. B* **80**, 104440 (2009).
- [36] P. Soin, A. P. Horsfield, and D. Nguyen-Manh, Efficient self-consistency for magnetic tight binding, *Comput. Phys. Commun.* **182**, 1350 (2011).
- [37] M. Mrovec, D. Nguyen-Manh, C. Elsässer, and P. Gumbsch, Magnetic Bond-Order Potential for Iron, *Phys. Rev. Lett.* **106**, 246402 (2011).
- [38] L. Ventelon and F. Willaime, Generalized stacking-faults and screw-dislocation core-structure in bcc iron: a comparison between *ab initio* calculations and empirical potentials, *Philos. Mag.* **90**, 1063 (2010).
- [39] V. L. Moruzzi and P. M. Marcus, Magnetovolume instabilities and ferromagnetism versus antiferromagnetism in bulk fcc iron and manganese, *Phys. Rev. B* **39**, 6957 (1989).
- [40] P. W. Ma, S. L. Dudarev, and J. S. Wróbel, Dynamic simulation of structural phase transitions in magnetic iron, *Phys. Rev. B* **96**, 094418 (2017).
- [41] J. Q. Zhao, H. Tian, Z. Wang, X. J. Wang, and J. W. Qiao, FCC-to-HCP phase transformation in CoCrNi<sub>x</sub> medium-entropy alloys, *Acta Metall. Sin. (Engl. Lett.)* **33**, 1151 (2020).
- [42] H. Ge and F. Tian, A review of *ab initio* calculation on lattice distortion in high-entropy alloys, *JOM* **71**, 4225 (2019).
- [43] T. Zuo, M. C. Gao, L. Ouyang, X. Yang, Y. Cheng, R. Feng, S. Chen, P. K. Liaw, J. A. Hawk, and Y. Zhang, Tailoring magnetic behavior of CoFeMnNiX ( $X = \text{Al, Cr, Ga, and Sn}$ ) high entropy alloys by metal doping, *Acta Mater.* **130**, 10 (2017).
- [44] I. Toda-Caraballo, J. S. Wróbel, D. Nguyen-Manh, P. Pérez, and P. E. J. Rivera-Díaz-del-Castillo, Simulation and modeling in high entropy alloys, *JOM* **69**, 2137 (2017).

- [45] S. Chiesa, P. M. Derlet, S. L. Dudarev, H. Van Swygenhoven, and H. Van Swygenhoven, Optimization of the magnetic potential for  $\alpha$ -Fe, *J. Phys. Condens. Matter* **23**, 206001 (2011).
- [46] M. Müller, P. Erhart, and K. Albe, Analytic bond-order potential for bcc and fcc iron—comparison with established embedded-atom method potentials, *J. Phys. Condens. Matter* **19**, 326220 (2007).
- [47] Y. S. Lin, M. Mrovec, and V. Vitek, Bond-order potential for magnetic body-centered-cubic iron and its transferability, *Phys. Rev. B* **93**, 214107 (2016).
- [48] S. L. Dudarev and P. M. Derlet, A ‘magnetic’ interatomic potential for molecular dynamics simulations, *J. Phys. Condens. Matter* **17**, 7097 (2005).
- [49] P. M. Derlet and S. L. Dudarev, Million-atom molecular dynamics simulations of magnetic iron, *Prog. Mater. Sci.* **52**, 299 (2007).
- [50] E. C. Stoner, Collective electron ferromagnetism II. Energy and specific heat, *Proc. R. Soc. Lond. A* **169**, 339 (1939).
- [51] L. D. Landau and E. M. Lifshitz, *Statistical Physics*, 3rd ed. (Pergamon Press, London, 1976).
- [52] P. W. Ma, C. H. Woo, and S. L. Dudarev, High-temperature dynamics of surface magnetism in iron thin films, *Philos. Mag.* **89**, 2921 (2009).
- [53] T. Mueller, A. Hernandez, and C. Wang, Machine learning for interatomic potential models, *J. Chem. Phys.* **152**, 050902 (2020).
- [54] I. Novikov, B. Grabowski, F. Kormann, and A. Shapeev, Magnetic moment tensor potentials for collinear spin-polarized materials reproduce different magnetic states of bcc Fe, *npj Comp. Mater.* **8**, 13 (2022).
- [55] J. H. Rose, J. R. Smith, F. Guinea, and J. Ferrante, Universal features of the equation of state of metals, *Phys. Rev. B* **29**, 2963 (1984).
- [56] P. Vinet, J. H. Rose, J. Ferrante, and J. R. Smith, Universal features of the equation of state of solids, *J. Phys. Condens. Matter* **1**, 1941 (1989).
- [57] P. Ravindran, L. Fast, P. A. Korzhavyi, B. Johansson, J. Wills, and O. Eriksson, Density functional theory for calculation of elastic properties of orthorhombic crystals: application to  $\text{TiSi}_2$ , *J. Appl. Phys.* **84**, 4891 (1998).
- [58] A. Togo and I. Tanaka, First principles phonon calculations in materials science, *Scr. Mater.* **108**, 1 (2015).
- [59] H. Geng, N. Chen, and M. Sluiter, First-principles equation of state and phase stability for the Ni-Al system under high pressures, *Phys. Rev. B* **70**, 094203 (2004).
- [60] H. Fujihisa and K. Takemura, Stability and the equation of state of alpha-manganese under ultrahigh pressure, *Phys. Rev. B* **52**, 13257 (1995).
- [61] X. Sha and R. E. Cohen, First-principles thermal equation of state and thermoelasticity of hcp Fe at high pressures, *Phys. Rev. B* **81**, 094105 (2010).
- [62] O. Gülseren, O. Gülseren, O. Gülseren, and R. E. Cohen, High-pressure thermoelasticity of body-centered-cubic tantalum, *Phys. Rev. B* **65**, 064103 (2002).
- [63] Y. Mishin, M. Mehl, D. Papaconstantopoulos, A. Voter, and J. Kress, Structural stability and lattice defects in copper: *ab initio*, tight-binding, and embedded-atom calculations, *Phys. Rev. B* **63**, 224106 (2001).
- [64] P. B. Roy and S. B. Roy, Applicability of three-parameter equation of state of solids: compatibility with first principles approaches and application to solids, *J. Phys. Condens. Matter* **15**, 1643 (2003).
- [65] Y. K. Huang and C. Y. Chow, The generalized compressibility equation of Tait for dense matter, *J. Phys. D. Appl. Phys.* **7**, 2021 (1974).
- [66] N. H. Mao, Empirical equation of state for high compression, *J. Geophys. Res.* **75**, 7508 (1970).
- [67] M. Kumari and N. Dass, An equation of state applied to sodium chloride and caesium chloride at high pressures and high temperatures, *J. Phys. Condens. Matter* **2**, 3219 (1990).
- [68] J. Freund and R. Ingalls, Inverted isothermal equations of state and determination of  $B_0$ ,  $B'_0$  and  $B''_0$ , *J. Phys. Chem. Solids* **50**, 263 (1989).
- [69] V. A. Lubarda, On the effective lattice parameter of binary alloys, *Mech. Mater.* **35**, 53 (2003).
- [70] N. Saunders and A. P. Miodownik, *CALPHAD (Calculation of Phase Diagrams): A Comprehensive Guide* (Pergamon Press, London, 1998), Vol. 1.
- [71] G. Kresse and J. Furthmüller, Efficiency of *ab-initio* total energy calculations for metals and semiconductors using a plane-wave basis set, *Comput. Mater. Sci.* **6**, 15 (1996).
- [72] G. Kresse and J. Furthmüller, Efficient iterative schemes for *ab initio* total-energy calculations using a plane-wave basis set, *Phys. Rev. B* **54**, 11169 (1996).
- [73] P. E. Blöchl, Projector augmented-wave method, *Phys. Rev. B* **50**, 17953 (1994).
- [74] J. P. Perdew, K. Burke, and M. Ernzerhof, Generalized Gradient Approximation Made Simple, *Phys. Rev. Lett.* **77**, 3865 (1996).
- [75] H. J. Monkhorst and J. D. Pack, Special points for Brillouin-zone integrations, *Phys. Rev. B* **13**, 5188 (1976).
- [76] O. Hegde, M. Grabowski, X. Zhang, O. Waseda, T. Hicel, C. Freysoldt, and J. Neugebauer, Atomic relaxation around defects in magnetically disordered materials computed by atomic spin constraints within an efficient Lagrange formalism, *Phys. Rev. B* **102**, 144101 (2020).
- [77] See Supplemental Material at <http://link.aps.org/supplemental/10.1103/PhysRevMaterials.6.043806> for the relationship between the MIP and the magnetic description of the Ginzburg–Landau approximation, the local ground state computed by DFT for the FM and AFM configurations at different  $b/a$  ratios and the tabulated expressions of the MIP for ferromagnetic iron.
- [78] K. Wang, W. Zhu, S. Xiao, J. Chen, and W. Hu, A new embedded-atom method approach based on the  $p$ th moment approximation, *J. Phys. Condens. Matter* **28**, 505201 (2016).
- [79] R. Ravelo, T. C. Germann, O. Guerrero, Q. An, and B. L. Holian, Shock-induced plasticity in tantalum single crystals: Interatomic potentials and large-scale molecular-dynamics simulations, *Phys. Rev. B* **88**, 134101 (2013).
- [80] S. M. Foiles, M. I. Baskes, and M. S. Daw, Embedded-atom-method functions for the fcc metals Cu, Ag, Au, Ni, Pd, Pt, and their alloys, *Phys. Rev. B* **33**, 7983 (1986).
- [81] M. Acet, H. Zähres, E. F. Wassermann, and W. Pepperhoff, High-temperature moment-volume instability and anti-Invar of  $\gamma$ -Fe, *Phys. Rev. B* **49**, 6012 (1997).
- [82] J. Crangle and G. C. Hallam, The magnetization of face-centred cubic and body-centred cubic iron + nickel alloys, *Proc. R. Soc. Lond. A* **272**, 119 (1963).

- [83] M. Šob, M. Černý, J. Pokluda, P. Šandera, and M. Friák, *Ab initio* calculations of elastic and magnetic properties of Fe, Co, Ni, and Cr crystals under isotropic deformation, *Phys. Rev. B* **67**, 035116 (2003).
- [84] D. H. Chung, Elastic moduli of single crystal and polycrystalline MgO, *Philos. Mag.* **8**, 833 (1963).
- [85] O. L. Anderson, A simplified method for calculating the Debye temperature from elastic constants, *J. Phys. Chem. Solids* **24**, 909 (1963).
- [86] J. J. Adams, D. S. Agosta, R. G. Leisure, and H. Ledbetter, Elastic constants of monocrystal iron from 3 to 500 K, *J. Appl. Phys.* **100**, 113530 (2006).
- [87] J. A. Rayne and B. S. Chandrasekhar, Elastic constants of iron from 4.2 to 300 °K, *Phys. Rev.* **122**, 1714 (1961).
- [88] B. J. Lee and M. I. Baskes, Second nearest-neighbor modified embedded-atom-method potential, *Phys. Rev. B* **62**, 8564 (2000).
- [89] D. J. Dever, Temperature dependence of the elastic constants in  $\alpha$ -iron single crystals: relationship to spin order and diffusion anomalies, *J. Appl. Phys.* **43**, 3293 (1972).
- [90] E. Asadi, M. Asle Zaeem, S. Nouranian, and M. I. Baskes, Quantitative modeling of the equilibration of two-phase solid-liquid Fe by atomistic simulations on diffusive time scales, *Phys. Rev. B* **91**, 024105 (2015).
- [91] S. A. Etesami and E. Asadi, Molecular dynamics for near melting temperatures simulations of metals using modified embedded-atom method, *J. Phys. Chem. Solids* **112**, 61 (2018).
- [92] A. M. Goryaeva, J. Dérès, C. Lapointe, P. Grigorev, T. D. Swinburne, J. R. Kermode, L. Ventelon, J. Baima, and M.-C. Marinica, Efficient and transferable machine learning potentials for the simulation of crystal defects in bcc Fe and W, *Phys. Rev. Materials* **5**, 103803 (2021).
- [93] H. Zhang, B. Johansson, and L. Vitos, *Ab initio* calculations of elastic properties of bcc Fe-Mg and Fe-Cr random alloys, *Phys. Rev. B* **79**, 224201 (2009).
- [94] V. I. Razumovskiy, A. V. Ruban, and P. A. Korzhavyi, First-principles study of elastic properties of Cr- and Fe-rich Fe-Cr alloys, *Phys. Rev. B* **84**, 024106 (2011).
- [95] G. Kresse and J. Hafner, *Ab initio* molecular dynamics for liquid metals, *Phys. Rev. B* **47**, 558 (1993).
- [96] V. Paidar, L. G. Wang, M. Šob, and V. Vitek, Study of the applicability of many-body central force potentials in NiAl and TiAl, *Model. Simul. Mater. Sci. Eng.* **7**, 369 (1999).
- [97] M. Mrovec, R. Gröger, A. G. Bailey, D. Nguyen-Manh, C. Elsässer, and V. Vitek, Bond-order potential for simulations of extended defects in tungsten, *Phys. Rev. B* **75**, 104119 (2007).
- [98] M. C. Marinica, F. Willaime, and J. P. Crocombette, Irradiation-Induced Formation of Nanocrystallites with C15 Laves Phase Structure in bcc Iron, *Phys. Rev. Lett.* **108**, 025501 (2012).
- [99] J. Byggmästar and F. Granberg, Dynamical stability of radiation-induced C15 clusters in iron, *J. Nucl. Mater.* **528**, 151893 (2020).
- [100] W. Xu and J. B. Adams, Fourth moment approximation to tight binding: application to bcc transition metals, *Surf. Sci.* **301**, 371 (1994).
- [101] A. K. Sinha, Topologically close-packed structures of transition metal alloys, *Prog. Mater. Sci.* **15**, 81 (1972).
- [102] P. Turchi, G. Treglia, and F. Ducastelle, Electronic structure and phase stability of A15 transition metals and alloys, *J. Phys. F Met. Phys.* **13**, 2543 (1983).
- [103] P. Olsson, C. Domain, and J. Wallenius, *Ab initio* study of Cr interactions with point defects in bcc Fe, *Phys. Rev. B* **75**, 014110 (2007).
- [104] P. K. Nandi, M. C. Valsakumar, S. Chandra, H. K. Sahu, and C. S. Sundar, Efficacy of surface error corrections to density functional theory calculations of vacancy formation energy in transition metals, *J. Phys. Condens. Matter.* **22**, 345501 (2010).
- [105] I. Valikova and A. V. Nazarov, Simulation of pressure effects on self-diffusion in bcc metals, *Defect Diffus. Forum* **277**, 125 (2008).
- [106] G. Simonelli, R. Pasianot, and E. J. Savino, Point-defect computer simulation including angular forces in bcc iron, *Phys. Rev. B* **50**, 727 (1994).
- [107] H. E. Schaefer, K. Maier, M. Weller, D. Herlach, A. Seeger, and J. Diehl, Vacancy formation in iron investigated by positron annihilation in thermal equilibrium, *Scr. Metall.* **11**, 803 (1997).
- [108] H. R. Schober, W. Petry, and J. Trampenau, Migration enthalpies in FCC and BCC metals, *J. Phys. Condens. Matter* **4**, 9321 (1992).
- [109] B. J. Lee, M. I. Baskes, H. Kim, and Y. Koo Cho, Second nearest-neighbor modified embedded atom method potentials for bcc transition metals, *Phys. Rev. B* **64**, 184102 (2001).
- [110] Y. N. Osetsky, A. G. Mikhin, and A. Serra, Study of copper precipitates in  $\alpha$ -iron by computer simulation I. Interatomic potentials and properties of Fe and Cu, *Philos. Mag. A* **72**, 361 (1995).
- [111] A. F. Calder and D. J. Bacon, A molecular dynamics study of displacement cascades in  $\alpha$ -iron, *J. Nucl. Mater.* **207**, 25 (1993).
- [112] M. S. Duesbery and V. Vitek, Plastic anisotropy in b.c.c. transition metals, *Acta Metall.* **46**, 1481 (1998).
- [113] S. L. Frederiksen and K. W. Jacobsen, Density functional theory studies of screw dislocation core structures in bcc metals, *Philos. Mag.* **83**, 365 (2003).